

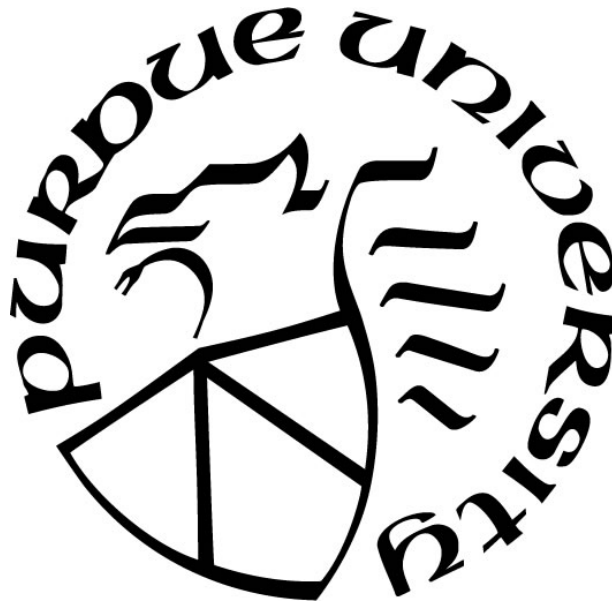
**DEFORMATION MECHANISMS IN UNIRRADIATED & IRRADIATED  
IRON CHROMIUM ALUMINUM IDENTIFIED BY TEM IN SITU  
TENSILE TESTING**

by  
**George Warren**

**A Thesis**

*Submitted to the Faculty of Purdue University  
In Partial Fulfillment of the Requirements for the degree of*

**Master of Science in Materials Engineering**



School of Materials Engineering  
West Lafayette, Indiana  
August 2021

**THE PURDUE UNIVERSITY GRADUATE SCHOOL**  
**STATEMENT OF COMMITTEE APPROVAL**

**Dr. Janelle Wharry, Chair**

School of Materials Engineering

**Dr. Anter El-Azab**

School of Materials Engineering & Nuclear Engineering

**Dr. Ernesto E Marinero**

School of Materials Engineering

**Dr. Yaqiao Wu**

Micron School of Materials Science & Engineering, Boise State University

**Approved by:**

Dr. David Bahr

*To my family who support me through everything*

## TABLE OF CONTENTS

LIST OF TABLES .....	6
LIST OF FIGURES .....	7
LIST OF ABBREVIATIONS .....	9
ABSTRACT .....	10
CHAPTER 1 INTRODUCTION .....	11
CHAPTER 2 BACKGROUND .....	13
2.1 FeCrAl .....	13
2.2 Deformation Processes in Body Centered Cubic (BCC) Crystals .....	13
2.3 Irradiation .....	15
2.3.1 Ion Irradiation .....	15
2.4 Microstructure .....	16
2.5 Micromechanical Testing .....	17
2.5.1 Nanohardness Test .....	17
2.5.2 TEM in situ Tensile Test .....	18
2.5.3 Size Effect .....	18
CHAPTER 3 METHODS .....	26
3.1 Stopping and Range of Ions in Matter (SRIM) .....	26
3.2 Dose and Damage .....	26
3.3 Microhardness .....	26
3.4 TEM Sample Creation .....	27
3.4.1 TEM Lamella Sample Creation .....	27
3.4.2 TEM in situ Tensile Test Specimen Creation .....	28
3.5 TEM Imaging & in situ Tensile Testing .....	28
CHAPTER 4 RESULTS .....	35
4.1 Microstructure .....	35
4.2 Nanohardness .....	35
4.3 Tensile Tests .....	36
4.3.1 Unirradiated [001] .....	36
4.3.2 Unirradiated [011] .....	37



4.3.3 Unirradiated [111] .....	37
4.3.4 Irradiated [001] .....	37
4.3.5 Irradiated [011] .....	38
4.3.6 Irradiated [111] .....	38
CHAPTER 5 DISCUSSION.....	54
REFERENCES .....	57

## LIST OF TABLES

Table 1 Composition and displacement energies used in SRIM simulation [41] .....	31
Table 2 Process and parameters for thinning TEM lamella for dislocation loop imaging .....	32
Table 3 Dimensions for unirradiated and irradiated tensile samples .....	34

## LIST OF FIGURES

Figure 1 CRSS is defined as the stress acting on the plane and in the direction that slip occurs. Slip will occur in the plane and direction with the least resistance to dislocation motion [16].	20
Figure 2 Stacking faults, produced by partial dislocations with $1/6\langle 111 \rangle$ character gliding in parallel planes, build upon one another. If an energy barrier is passed, a stable twin is formed and can grow [17].	21
Figure 3 As a crystal slips, the orientation remains constant through the slipped planes (a). When twinning occurs, the crystal orientation above and below the twinning plane is changed (b) [16].	22
Figure 4 The damage profile produced by different irradiating particles. The damage profile depends on parameters such as the irradiating particle energy, size and charge [25].	23
Figure 5 Four FeCrAl alloys irradiated with neutrons to between 0.3 – 0.8 DPA at temperatures between 335°C - 355°C. Dislocation loops with $a/2\langle 111 \rangle$ and $a\langle 100 \rangle$ character along with dislocation line networks are present [29].	24
Figure 6 Four FeCrAl alloys with 10 – 18 wt% Cr and 2.9 – 4.9 wt% Al neutron irradiated to 1.8 DPA at 382°C for the purpose of studying microstructure and mechanical properties as a function of alloy composition [10].	25
Figure 7 Ion irradiation damage profile with respect to depth as calculated from SRIM simulation. A depth of 400nm – 600nm was targeted for mechanical properties in this study (highlighted in blue).	30
Figure 8 TEM in situ tensile sample fabrication process. (a) Location identification / sample outline, (b) FIB milling, (c) sample extraction from bulk, (d) push to pull device and location for sample placement, (e) & (f) thinning to specific depth and (g) final thinned and dogbone shaped sample [43].	33
Figure 9 EBSD image displaying the grain structure and size of FeCrAl.	39
Figure 10 TEM lamella imaged using BFSTEM down the 011 zone axis. It was decided that the distributed spots were caused by FIB milling.	40
Figure 11 (left) TEM lamella imaged using BFSTEM down the 011 zone axis and (right) dislocation loops imaged 600nm into the irradiated surface.	41
Figure 12 Unirradiated & irradiated FeCrAl microstructural data superimposed on graph displaying the relationship between extrinsic and intrinsic size effect from [43].	42
Figure 13 Nanohardness tests done on two FeCrAl alloys with 5wt% Al (red) and 7wt% Al (blue) displaying the irradiation induced hardening.	43
Figure 14 (above) Tensile test for unirradiated 001 grain orientation exhibiting failure after linearly deforming. (below) Still images from BFTEM video at the beginning of test and after failure.	44

Figure 15 (above) Tensile test for unirradiated 001 grain orientation exhibiting failure after linearly deforming. (below) Still images from BFTEM video at the beginning of test and after failure. .	45
Figure 16 (above) Tensile test for unirradiated 001 grain orientation exhibiting failure after yielding. (below) Still images from BFTEM video at the beginning of test and after failure.....	46
Figure 17 (above) Tensile test for unirradiated 011 grain orientation exhibiting failure after linearly deforming. (below) Still images from BFTEM video at the beginning of test and after failure. .	47
Figure 18 (above) Tensile test for unirradiated 011 grain orientation exhibiting many slip events during plastic deformation. (below) Still images from BFTEM video corresponding to beginning, yield, slip, and failure.....	48
Figure 19 (above) Tensile test for unirradiated 111 grain orientation exhibiting twinning and slip. (below) Still images from BFTEM video corresponding to beginning, yield, twin formation, slip, and failure. ....	49
Figure 20 (above) Tensile test for irradiated 001 grain orientation exhibiting failure after yielding. (below) Still images from BFTEM video at the beginning of test and after failure.....	50
Figure 21 (above) Tensile test for irradiated 011 grain orientation exhibiting failure after yielding. (below) Still images from BFTEM video at the beginning of test and after failure.....	51
Figure 22 (above) Tensile test for irradiated 111 grain orientation exhibiting slip and softening. (below) Still images from BFTEM video corresponding to beginning, yielding, slip and failure. ....	52
Figure 23 (above) Tensile test for irradiated 111 grain orientation exhibiting slip and slight hardening. (below) Still images from dark field TEM (DFTEM) video corresponding to beginning yield, slip and failure.....	53

## **LIST OF ABBREVIATIONS**

FeCrAl – Iron Chromium Aluminum

ATF – Accident Tolerant Fuel

nm – Nanometer

um – Micrometer

TEM – Transmission Electron Microscope

BCC – Body Centered Cubic

CRSS – Critical Resolved Shear Stress

PKA – Primary Knock on Atom

DPA – Displacement per Atom

BFSTEM – Bright Field Scanning Transmission Electron Microscopy

SRIM – Stopping and Range of Ions in Matter

FIB – Focused Ion Beam

FEG – Field Emission Gun

STEM – Scanning Transmission Electron Microscopy

BFTEM – Bright Field Transmission Electron Microscopy

CAES – Center for Advanced Energy Studies

SEM – Scanning Electron Microscope

EBSD – Electron Backscatter Diffraction

EELS – Electron Energy Loss Spectroscopy

DFTEM – Dark Field Transmission Electron Microscopy

## ABSTRACT

FeCrAl alloys are being investigated as candidate materials for replacing zirconium based alloys as nuclear reactor fuel cladding because of their superior high temperature oxidation resistance in steam environments. Unirradiated FeCrAl as well as Fe<sup>2+</sup> ion irradiated FeCrAl to a peak dose of 20DPA were mechanically tested and compared against each other. Nanohardness tests were performed on both the unirradiated and irradiated conditions and it was found that the irradiated alloy was about 1GPa harder than its unirradiated counterpart. TEM *in situ* tensile tests were performed using the Bruker push to pull device alongside a PI95 Picoindenter on single crystals with grain orientations 001, 011 and 111. The unirradiated 001 grains tended to fail without yielding in a brittle manner while the irradiated 001 grain yielded and reached an ultimate tensile strength before failure. The unirradiated 011 grains behaved in a mixed manner, where one failed without yielding and one slipped many times before failing. The irradiated 011 grain yielded and failed quickly thereafter. The unirradiated 111 grain yielded, slipped and twinned before failing and both irradiated 111 grains slipped. Two general trends were observed. One, each unirradiated single grain was stronger than its irradiated counterpart. This trend is indicative of the ion irradiated microstructure facilitating bulklike mechanical behavior in the irradiated samples whereas the unirradiated samples exhibited mechanical size effects due to either the total lack of preexisting defects or the ability for existing defects to escape easily to the surface of the sample resulting in a pristine, defect free sample. Two, regardless of irradiation condition, the 001 grain orientation was brittle, the 011 grain orientation deformed in a mixed brittle/ductile manner and the 111 grain orientation was ductile through all tests. These results are indicative of the geometry of the BCC crystal structure and the slip system involving these orientations.

## CHAPTER 1 INTRODUCTION

The increasing demand for clean renewable energy has placed a great strain on energy produced by burning fossil fuels such as coal. According to the U.S. Energy Information Administration, as of 2019 petroleum, natural gas and coal made up about 80% of the nation's energy while only about 8% was made from nuclear power plants. While burning fossil fuels makes up a great amount of the energy produced worldwide, nuclear power production holds the only practical key to safely and affordably aiding or possibly replacing fossil fuels. There are several hurdles that must be addressed when it comes to nuclear power but one in particular is winning the trust of the public as it relates to the safety and security of nuclear power plants. After the unforeseeable disastrous accident at the Fukushima Daiichi nuclear reactor in 2011, many in the scientific community began working on solutions to safeguard against such accidents. One such solution is increasing the amount of response time for officials and professionals to regain control or provide mitigation efforts if such a problem should occur [1]. To achieve this goal, new materials are being researched with the hope that they will replace the currently used materials that make up the reactor. Iron chromium aluminum (FeCrAl) alloys are being researched for potentially replacing existing zirconium based alloys as an accident tolerant fuel (ATF) cladding material. FeCrAl's superior resistance to high temperature oxidation at temperatures greater than 1500C due to a stable alumina oxide film that coats and shields the surface of the material makes it an attractive alloy for further research [2]. A great challenge associated with understanding a materials response to a nuclear reactor environment is the unique type of damage that occurs in a material due to the radiation it incurs while in use. This damage is primarily caused by the collisions between neutrons and the atoms within the materials makeup. Irradiating a material with neutrons to damage levels suitable for research can take months or even years and it can be quite costly, not to mention the restrictions that come with handling radioactive materials. An alternative to neutron irradiation is ion irradiation which, for a variety of damage levels, is much quicker and is less costly than using neutrons and reduces radioactivity to background levels [3–5]. One drawback to using ions instead of neutrons to irradiate the material is the extremely shallow damage depth ions are capable of producing. The depth ions are able to penetrate, and thus damage, is on the order of nanometers (nm) to a few micrometers ( $\mu\text{m}$ ) which makes targeting this damaged zone difficult to test. Small scale *in situ* transmission electron microscopy (TEM) micromechanical testing provides a great

way to test these small volumes and also directly observe the deformation process in real time [6,7]. This allows the researcher to capture mechanical data while simultaneously comparing with visual observations, coupling the two, creating a powerful tool. In this study the competition between slip and twinning will be considered in single crystal FeCrAl specimen as well as their mechanical properties. The size of the specimen is a point of emphasis due to the potential size effect that is associated with small scale mechanical testing in unirradiated and irradiated samples [6]. The Bruker push to pull device is used to perform tensile tests on nm sized sample and it will be established for the first time that these tests are effective in providing useful information such as mechanical data and deformation behaviors in FeCrAl alloys.



## CHAPTER 2 BACKGROUND

### *2.1 FeCrAl*

The harsh environments associated with fuel cladding in a nuclear reactor, such as neutron bombardment and high stresses while operating at high temperatures for long durations of time are concerning due to the detrimental effects these environments may have on the mechanical performance of the cladding material [8,9]. FeCrAl is a candidate alloy being considered for use in current and future nuclear reactors as an ATF cladding material replacement. Low chromium FeCrAl alloys offer superior resistance to oxidation at high temperatures ( $>1500^{\circ}\text{C}$ ) when compared to zirconium based alloys currently used as fuel cladding due to a stable alumina oxide thin film that forms on the surface of the material [2,10]. FeCrAl's resistance to oxidation at elevated temperatures increases the available response time in the event of an accident for mitigation purposes. In addition to oxidation resistance, ferritic iron chromium alloys tend to resist irradiation induced swelling which can extend the lifetime for the component [11–13].

### *2.2 Deformation Processes in Body Centered Cubic (BCC) Crystals*

Plastic deformation in BCC metals and alloys is associated with the deviation from linearly elastic deformation, known as the yield, and the flow of dislocations and / or the formation of deformation twins in the crystal lattice. These deformation modes are dependent on loading direction, crystallographic orientation, strain rate and temperature [14,15]. BCC structured materials tend to slip along planes and directions of high atomic density, known as slip systems. These slip systems are all in the  $\langle 111 \rangle$  direction on the  $\{110\}$ ,  $\{211\}$ , and  $\{321\}$  planes. The reason for this behavior is that the atomic distortion in these planes along these directions, when a dislocation glides, is minimized [15,16]. The high number of slip systems that exist in BCC materials enable slip to occur readily and thus these materials tend to be ductile. When a single crystal slips, the slip occurs in the direction of the dislocations Burgers vector which, in an edge dislocation, is perpendicular to the dislocation line and in a screw dislocation, is parallel to the dislocation line. During deformation, slip in a single crystal will occur in the direction and on the plane that is most favorable for slip. The stress that the slip ultimately occurs at is referred to as the critical resolved

shear stress (CRSS) [16]. An important note is that the crystal orientation above and below the slip plane remains unchanged from the undeformed crystal orientation prior to slip. The CRSS (Equation 1),  $\tau_R$ , is a function of the applied stress,  $\sigma$ , and the angles between the applied stress and the plane and direction of slip,  $\varphi$  and  $\lambda$ , respectively.

$$\tau_R = \sigma \cos \varphi \cos \lambda \quad \text{Eq 1}$$

A diagram is shown below in Figure 1 displaying the CRSS. From Equation 1, if both the angle between the slip plane and the applied stress and the angle between slip direction and the applied stress are both 45 degrees, the shear stress on the slip plane will be maximized. Furthermore, if either of these angles is 90 degrees to the applied stress, the shear stress on the slip plane will be nonexistent.

When dislocations move in a plastically deforming metal or alloy, they will eventually reach obstacles such as interstitials, other dislocations, and grain boundaries etc. which impede their motion. Hardening occurs when the impedance of dislocation motion results in dislocations piling up. As dislocations pile up, larger stresses are required for dislocations to flow. Eventually the dislocation pile up will become so great that no dislocations are able to flow. These large stresses can lead to another type of deformation mode called deformation twinning [17]. Twinning causes a reorientation of the crystal relative to the parent crystal orientation and happens on the  $\{211\}$  planes in the  $\langle 111 \rangle$  directions [16,18–20]. These directions and planes are preferred for stacking fault formation by way of partial dislocations over full dislocation slip in the  $\langle 111 \rangle \{110\}$  and  $\langle 111 \rangle \{321\}$  systems [21]. During twinning, the displacement of each atomic plane within the twinned crystal region is proportional to the distance from the twinning plane leading to a mirrored crystal with respect to the twinning plane [16]. Many proposed nucleation processes share a common idea that partial dislocations are responsible for first nucleating and then growing twins [18–20]. One proposed mechanism is shown below in Figure 2 where the partial dislocation, or twinning dislocation, with character  $1/6\langle 111 \rangle$  nucleates at a position of high stress (edge/surface of nanowire) and glides, leaving behind a stacking fault. When the partial dislocation is nucleated and glides, a stress drop is typically observed and, upon further deformation, more partial dislocations are nucleated and glide in consecutive parallel planes. If an initial energy barrier is

overcome, the subsequent nucleated partial dislocations will cause the twinned region to grow at stresses relatively small compared to the stress required to nucleate the initial partial dislocation. As the partial dislocations reach the other surface of the nanowire, the twinned region may continue to grow due to the nucleation of more partial dislocations at the twin boundaries [17].

The reoriented grain, or twinned grain, tends to be preceded by microcracking and also potentially provides new slip systems that are favorable for slip to occur [16,18,22–24]. Figure 3 shows a comparison between deformation slip and deformation twinning. Highlighted are the unchanged crystal orientation in deformation slip (blue region in (a)) and the reoriented crystal in deformation twinning (yellow region in (b)).

### *2.3 Irradiation*

During irradiation, neutrons or ions are accelerated toward a material and transfer their energy into the incident material by way of collisions with lattice atoms. If the irradiating particle has sufficient energy when the collision occurs, the lattice atom, or primary knock on atom (PKA), will be displaced and potentially collide with other lattice atoms. This process of displaced atoms displacing other atoms is known as the damage cascade. As a material is irradiated, large quantities of vacancies and interstitials are created from cascades. These introduced defects are responsible for altering the mechanical properties of the material and tend to produce a hardening effect due to the coalescence of point defects into higher dimensional defects such as clusters, dislocation loops, bubbles and voids [10]. The relevant defects will be described in more detail in following section.

#### *2.3.1 Ion Irradiation*

Heavy ions ( $\text{Fe}^{2+}$ ) were used as the irradiating particle to study the effect of irradiation on the mechanical performance of FeCrAl. Although the damage profile within the material is morphologically different when using ions instead of neutrons as the irradiating particle (Figure 4), the microstructure produced consists of the same variety of defects [25]. Aside from mimicking the damage caused by neutrons, ion irradiation provides three additional benefits: One, ion

irradiation does not produce a radioactive sample. Radioactive samples present a host of challenges such as health hazards, complications associated with transporting samples, availability of facilities capable of handling radioactive samples, and the expenses associated with the previously mentioned challenges. Ion irradiated samples alleviate all of these challenges. Two, experimental parameters are easily controlled through ion irradiation. The strict controlling of these parameters allows for fundamental processes and mechanisms to be studied. Three, high displacements per atom (DPA) samples can be produced in a relatively short period of time. High DPA neutron irradiated samples can take months or years to produce while high DPA ion irradiated samples can take hours [26,27]. One drawback to using ion irradiation instead of neutron irradiation is the extremely shallow penetration depth at which the damage occurs. The reason for the difference in penetration depth between ion and neutron irradiation is the interactions between the particles and the incident material. Neutrons, being uncharged, are able to pass through the material unimpeded until a direct collision is made with a lattice atom. This enables the neutron to travel much further into the material. Ions on the other hand are charged and so they are either attracted or repelled from the lattice atoms and collisions between the two are more likely to occur [28]. This penetration depth, on the order of nm to tens of  $\mu\text{m}$ , makes mechanical testing difficult. Explained in the micromechanical testing section, TEM *in situ* tensile testing provides a unique solution to this problem.

## 2.4 Microstructure

FeCrAl has been shown to develop microstructural features such as dislocation networks, dislocation loops, black dots, and solute clustering as a result of irradiation. Bright field scanning TEM (BFSTEM) images of these defects are shown below in Figure 5 and Figure 6. These microstructures are important as they relate directly to the mechanical behavior [9,10,29–31]. When stress is applied to the material, these defects can act as barriers to dislocation motion. This blocking of dislocation motion can manifest itself as hardening or softening of the material. The localization of high and low density areas of defects can also occur and this can lead to large variations of mechanical behavior in small scale mechanical tests. In small scale tests this may happen because of the small volume of material being tested and the chance of defects either existing or not existing within that volume. In addition to blocking dislocations, these defects can

act as dislocation sources because of the high concentrated stresses that build up at the defect sites. Dislocations strengthen the material by becoming tangled with one another producing dislocation networks which reduce or disable their ability to flow and cause plastic deformation. Conversely, softening has also been observed in low temperature irradiation [32]. Dislocation networks have also been shown to influence the size, density and ratio of dislocation loop formation. Dislocation loops in FeCrAl develop in two different orientations,  $a/2\langle 111 \rangle$  and  $a\langle 100 \rangle$  and can be mobile or immobile. The interactions between these defects play a significant role in the strengthening [9,10,14,29,33].

## *2.5 Micromechanical Testing*

Small scale testing methods such as pillar compression, cantilever bending, and tensile stressing are testing methods that probe the mechanical performance of materials with nm or um dimensions. These experiments shed light on fundamental processes such as deformation mechanisms and provide a tool for studying the effects of grain boundary interactions and, in the case of the current study, single crystal behavior and the shallow irradiated volumes produced by ion irradiation. Hardness measurements using indentation along with a special TEM testing method are used in this study to quantify and observe mechanical deformation as it takes place. Because the small size of the samples makes them susceptible to a size effect, it is important to understand what can influence mechanical data with respect to their small sizes. The next three sections will provide information on the testing methods used as well as an introduction to size effects and causes for these behaviors.

### *2.5.1 Nanohardness Test*

Nanohardness test are performed on unirradiated and irradiated materials to measure the degree of hardening caused by irradiation. This is achieved by measuring the hardness vs depth in both conditions and then taking the difference in hardness between the two conditions. The difference in hardness is then a quantification of the irradiation induced hardening [34]. A variety of geometries exist for the size and shape of the indenter tip, including pyramid, cone and ball tips with varying radii.

### 2.5.2 TEM *in situ* Tensile Test

To understand the effect of irradiation on the mechanical response of FeCrAl, it is important to isolate and test only the irradiated material. This ensures that the data acquired is a direct result from the damaged zone. The size of the damaged volume in an ion irradiated sample, as mentioned above, is quite small which makes conventional mechanical testing challenging or even impossible. Using the TEM to perform mechanical tests provides a solution to testing small volumes of material while also providing the advantage of observing deformation processes and comparing those events with mechanical data as they occur. Cross referencing data such as stress increases / decreases, or strain bursts, with observed plastic occurrences such as slip, dislocation pile ups, and twin formations is a unique advantage provided by *in situ* TEM micromechanical testing.

### 2.5.3 Size Effect

It is commonly seen in mechanical testing that when the limiting dimension of the sample nears the characteristic defect spacing, data such as yield strength increase rapidly and may even approach theoretical values. This is an important aspect to consider when testing irradiated samples because the density of defects produced by the irradiation process compared to the defect density prior to irradiation effectively causes a reduction in the average spacing between defects, mitigating the size effect [6,7,35]. To gain meaningful information about the mechanical performance, it is important to understand the reasons for increased strengths, stress drops, serrated flow and strain hardening or softening. As plastic deformation is a consequence of the movement of dislocations, dislocations must first exist. Defects act as dislocation generating sites, or sources, and dislocation barriers. The increased strength can be caused by the pinning and building up of dislocations at barriers. The building up of dislocations at a barrier causes stress concentrations at those location and ultimately the barrier is bypassed and enables a flood of dislocations to become mobile. This process is known as a dislocation avalanche which manifests itself as a strain burst or load drop. Strain bursts can lead to disproportionate increases in strain and ultimately catastrophic material failure [36]. Another type of size effect is the stochastic behavior of yield strength. Due to the size of the sample, which is on the same order of magnitude as the length

between defects, there is a likelihood that few to no dislocations will exist. For plastic deformation to occur without preexisting dislocations, dislocations must first be nucleated which requires stresses near the theoretical yield stress. The lack of existing dislocations is referred to dislocation starvation. Furthermore, because the sample surface is relatively close by, these newly nucleated dislocations can escape to the surface quickly and easily which results in the defect free sample again [37]. Source truncation is another explanation for scattered yield strengths. In source truncation, where the stress necessary for dislocation nucleation is inversely related to the length of the source, the samples weakest source must first be activated for yielding to occur. In small samples, the weakest source will not always be the same from sample to sample which can cause a large variation in observed strengths [38,39].

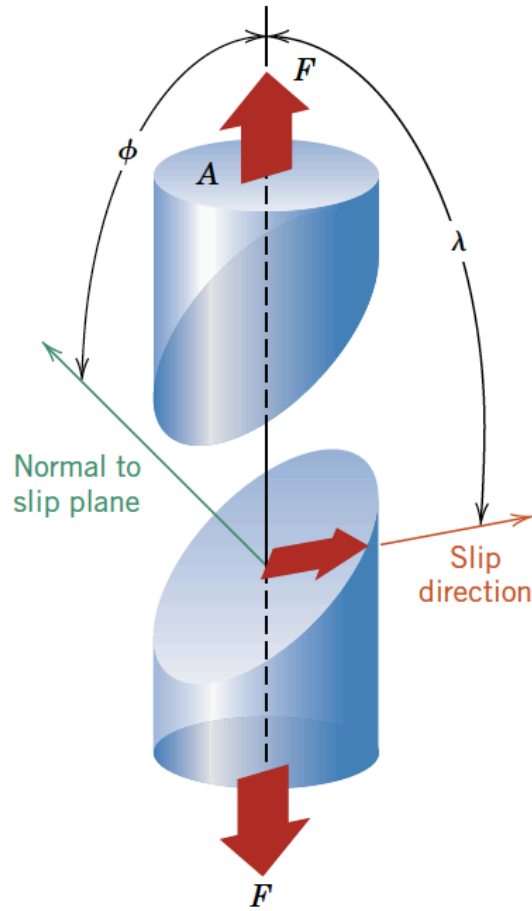


Figure 1 CRSS is defined as the stress acting on the plane and in the direction that slip occurs. Slip will occur in the plane and direction with the least resistance to dislocation motion [16].



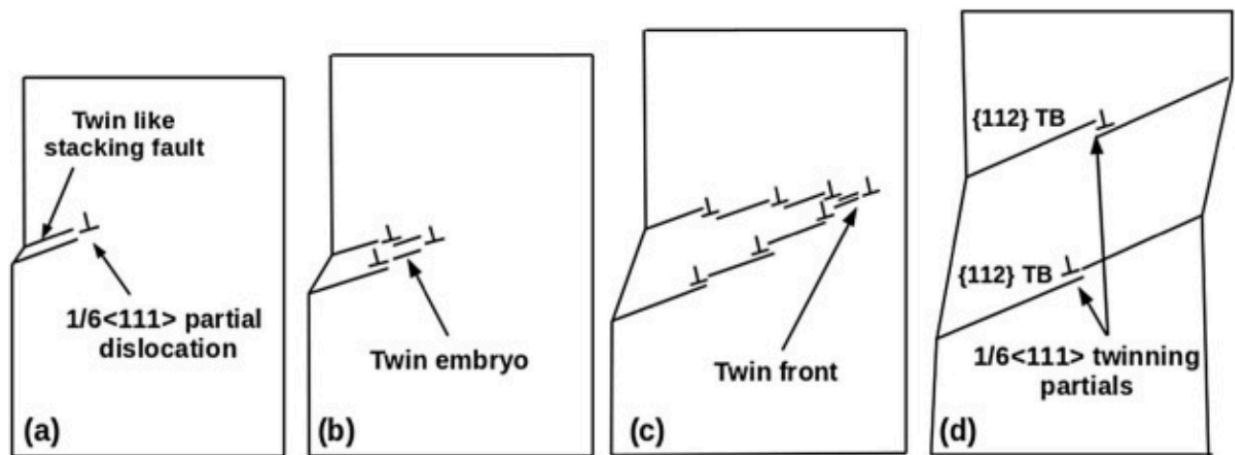


Figure 2 Stacking faults, produced by partial dislocations with  $1/6\langle 111 \rangle$  character gliding in parallel planes, build upon one another. If an energy barrier is passed, a stable twin is formed and can grow [17].

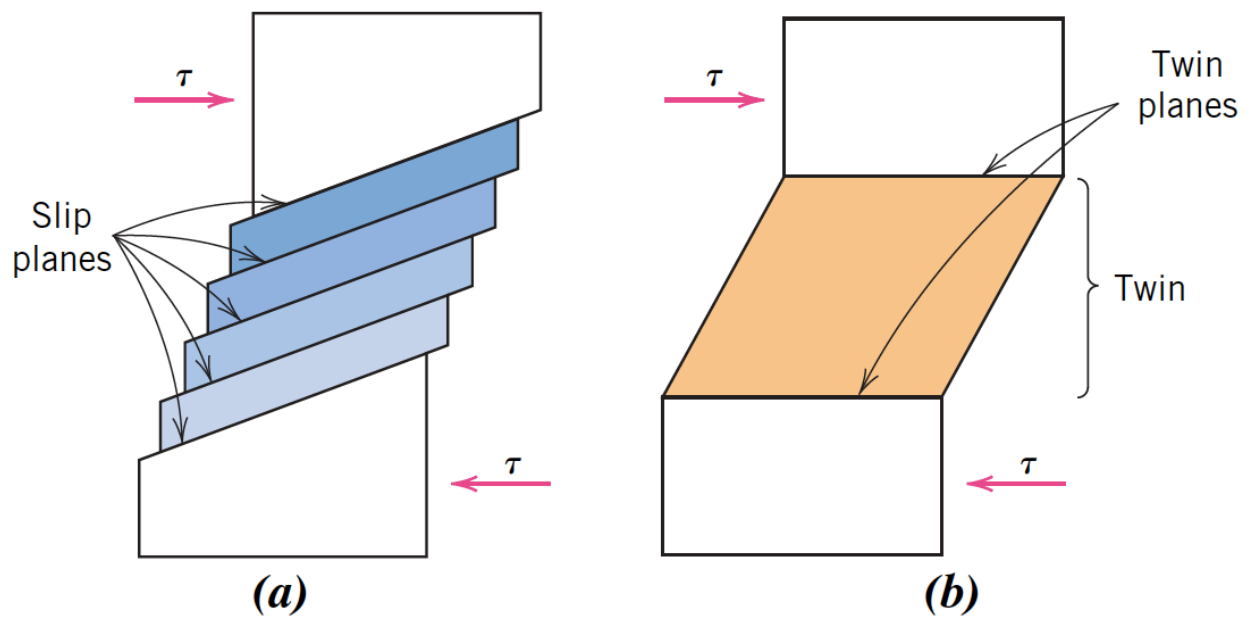
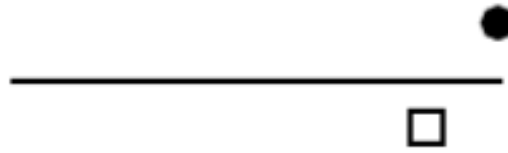


Figure 3 As a crystal slips, the orientation remains constant through the slipped planes (a). When twinning occurs, the crystal orientation above and below the twinning plane is changed (b) [16].

1 MeV electrons  
 $\bar{T} = 60 \text{ eV}$   
 $\varepsilon = 50\text{--}100\%$



1 MeV protons  
 $\bar{T} = 200 \text{ eV}$   
 $\varepsilon = 25\%$



1 MeV heavy ions  
 $\bar{T} = 5 \text{ keV}$   
 $\varepsilon = 4\%$



1 MeV neutrons  
 $\bar{T} = 35 \text{ keV}$   
 $\varepsilon = 2\%$

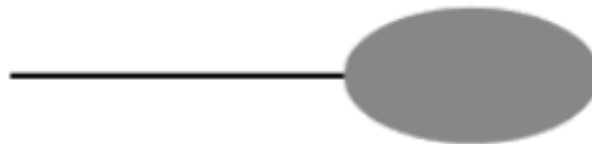


Figure 4 The damage profile produced by different irradiating particles. The damage profile depends on parameters such as the irradiating particle energy, size and charge [25].

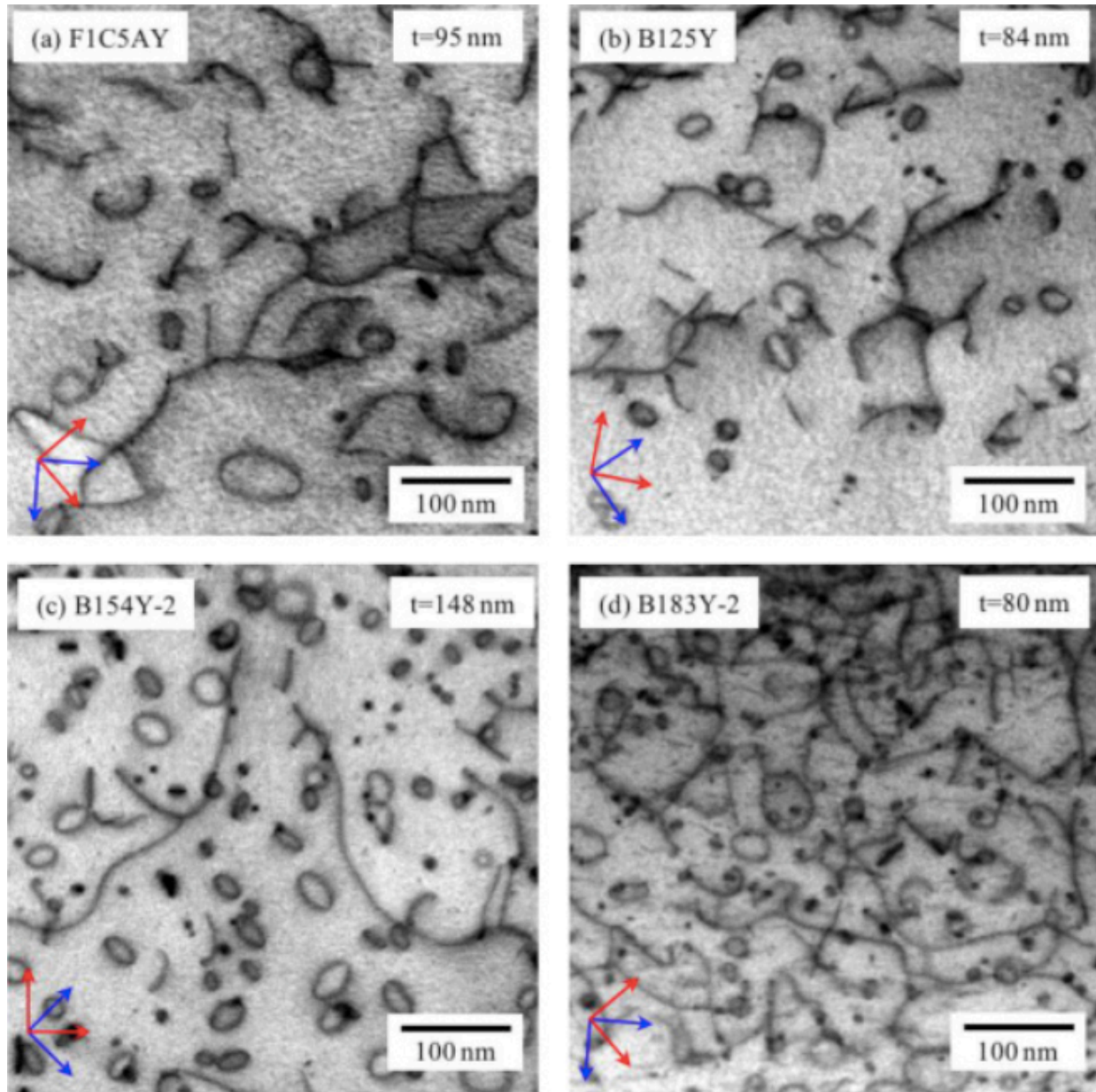


Figure 5 Four FeCrAl alloys irradiated with neutrons to between 0.3 – 0.8 DPA at temperatures between 335C° - 355C°. Dislocation loops with  $a/2\langle 111 \rangle$  and  $a\langle 100 \rangle$  character along with dislocation line networks are present [29].

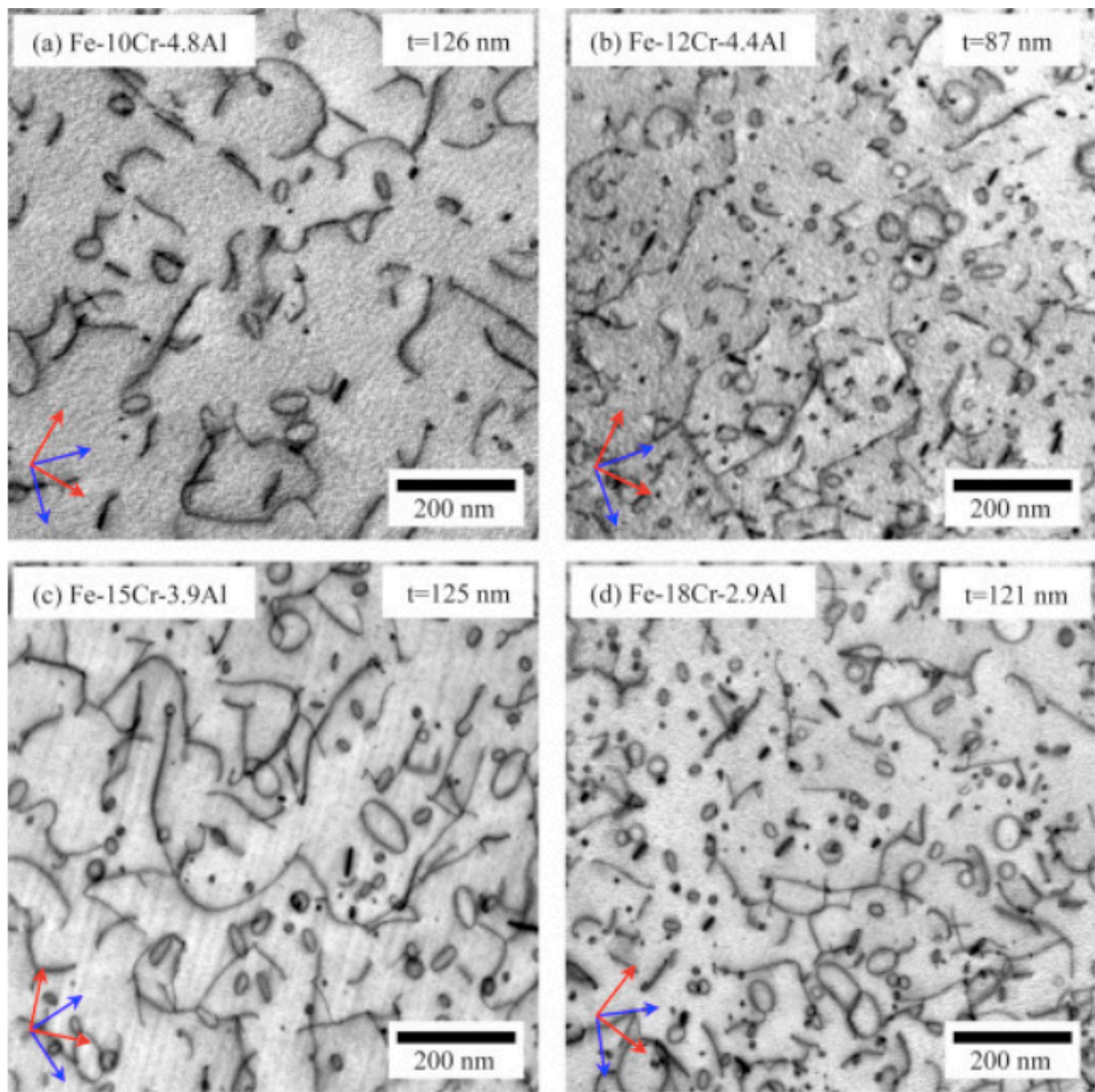


Figure 6 Four FeCrAl alloys with 10 – 18 wt% Cr and 2.9 – 4.9 wt% Al neutron irradiated to 1.8 DPA at 382°C for the purpose of studying microstructure and mechanical properties as a function of alloy composition [10].

## CHAPTER 3 METHODS

### 3.1 Stopping and Range of Ions in Matter (SRIM)

SRIM was used to model the damage in FeCrAl alloy with  $\text{Fe}^{2+}$  heavy ions accelerated with 4.4 MeV. Both the Brandt – Kitagawa approximation and the Bethe – Bloch theory are used for calculating the stopping powers for heavy ions with energies greater than 1MeV and Z's greater than 3 [40]. The damage profile is shown in Figure 7 and the at% and displacement energies for each alloying element used in the SRIM simulation are shown in Table 1.

### 3.2 Dose and Damage

The targeted damage for this study was 7 DPA at a depth of 400 – 600 nm. The maximum damage achieved was about 20 DPA at just over 1.5um depth. The calculated damage depends on the current of the ion beam which is calculated using the total charge that is applied to the specimen. The simulation software then provides  $10^6$  counts/coulomb to each microcoulomb arbitrarily and, using Equation 2, the damage is calculated.

$$DPA = \frac{\text{counts} \times R_d \left( \frac{\text{Displacements}}{\text{angstroms.ion}} \right)}{N \left( \frac{\text{atoms}}{\text{cm}^3} \right) \times q \left( \frac{\text{C}}{\text{ion}} \right) \times \text{Area}(\text{cm}^2) \times \left( \frac{\text{counts}}{\text{C}} \right)} \quad \text{Eq 2}$$

In the above equation, N is the atomic density, q is the charge of each ion, area refers to the irradiated area, or the aperture area, and  $R_d$  is the displacement rate which is calculated by SRIM software.

### 3.3 Microhardness

An iMicro Nanoindenter was used to perform nanoindentation to a depth of 2000nm at a constant displacement rate of 0.2nm/s using indent to maximum depth mode. The indenter geometry used was a Berkovitch tip. Several indents were made in random locations throughout the bulk sample

in both the unirradiated and irradiated samples. The hardness data was averaged and plotted against depth to show the hardening effect of the irradiation.

### *3.4 TEM Sample Creation*

All TEM samples were made using focused ion beam (FIB) processing. Imaging and tensile testing was done using an FEI Tecnai G<sup>2</sup> TF30 – Field Emission Gun (FEG) STwin scanning transmission electron microscope (STEM). TEM lamella were imaged using basic bright field TEM (BFTEM) imaging and BFSTEM imaging. The STEM imaging was done down the low zone axis with respect to the grain orientation of the sample being imaged. The TEM mechanical specimen were also imaged using basic BFTEM and BFSTEM prior to testing. The creation of the TEM lamella and tensile specimen are explained further in the following sections.

#### *3.4.1 TEM Lamella Sample Creation*

TEM lamella were made using basic FIB milling processing at the Center for Advanced Energy Studies (CAES) using a FEI Quanta 3D FEG FIB. To protect the surface of the sample from FIB damage, whether unirradiated or irradiated, a platinum bar was deposited above where the TEM lamella was to be made. The dimensions of the platinum bar were 14 $\mu$ m x 2 $\mu$ m x 6 $\mu$ m and it was deposited using 0.1nA. The operating voltage and current in the scanning electron microscope (SEM) were kept constant at 20kV and 1.9nA, respectively. The operating voltage in the FIB was kept constant at 30kV while the current ranged from 7nA to 48pA. The strength of the current was dependent on the precision needed for milling. For example, once the lamella was thinned below 500nm, the current was reduced from 0.5nA to 0.3nA and again reduced once the sample was thinned below 250nm from 0.3nA to 0.1nA. Standard TEM lift out techniques were used, such as trenching, thinning and under cutting, to extract the lamella from the bulk material and place onto the TEM copper grid [41]. Once the lamella was welded to the copper grid using platinum, thinning was performed on the lamella until it was electron transparent. This process was done at alternating between an angle of 50.5 and 53.5 such that when the lamella either reached or was less than 100 nm thick OR a hole began forming within the desired imaging area, thinning was stopped, and final cleaning was done. To remove FIB damage, a final cleaning process was performed. The

cleaning process consisted of exposing the entire lamella to a FIB rectangle at low voltage and low current for a specified amount of time. For a comprehensive understanding of the thinning process, Table 2 shows the voltages, current and corresponding thicknesses at which the sample was thinned.

### *3.4.2 TEM in situ Tensile Test Specimen Creation*

FIB machining was used to fabricate the tensile specimens using a FEI Quanta 3D FEG SEM/FIB at CAES as well as at Purdue University. Grain orientations were identified using electron backscatter diffraction (EBSD) detector and EDAX software. Platinum depositions were used to protect and define rough specimen edges. The platinum depositions were spaced approximately 4 $\mu$ m apart and trenches with dimensions 10 $\mu$ m x 8 $\mu$ m x 4 $\mu$ m were milled on either side of the depositions. The card with approximate dimensions 8 $\mu$ m x 6 $\mu$ m x 4 $\mu$ m was extracted from the bulk using a micro manipulator needle (OmniProbe) after undercutting and welded onto a Bruker push to pull device. The sample was attached to the push to pull device such that it could be thinned and shaped using FIB. The final thickness target was 100nm and the gauge length and width target were 1.5 $\mu$ m and 1 $\mu$ m, respectively. The gauge length and width measurements were obtained using an FEI Tecnai G<sup>2</sup> TF30 – FEG STwin STEM at CAES and the thickness was measured using Gatan Electron Energy Loss Spectroscopy (EELS). This unique process allows for a targeted testing depth as shown in Figure 8 (e) & (f). This is advantageous for this study because of the shallow ion irradiated penetration depth described earlier. Specific details of tensile specimen production are laid out in [42]. Figure 8 shows the process from start to finish. The final dimensions for the tested specimens are shown in Table 3. The asterisk in Table 3 represents the fact that the thickness was estimated for this sample. It is important to note that in the TEM, the sample appeared to be thick. 100nm was used as an estimate for the thickness because it made calculations simple.

### *3.5 TEM Imaging & in situ Tensile Testing*

The tension experiments were carried out on the same TEM as mentioned above (FEI Tecnai G<sup>2</sup> TF30 – FEG STwin STEM) at 300 kV accelerating voltage using a Bruker PI – 95 Picoindenter



and a 20um flat punch tip. The sample was tilted to the low zone axis corresponding to the sample being tested for BFTEM imaging and diffraction patterns were obtained for crystal orientation confirmation. Images were taken throughout the beam for microstructural characterization. One experiment was done in dark field mode while the rest were performed in bright field mode. The software used to run the tests was TriboScan which collects the mechanical data along with video of the test being carried out. The samples were stressed until failure occurred at a constant displacement rate of  $1\text{nm}\cdot\text{s}^{-1}$ .

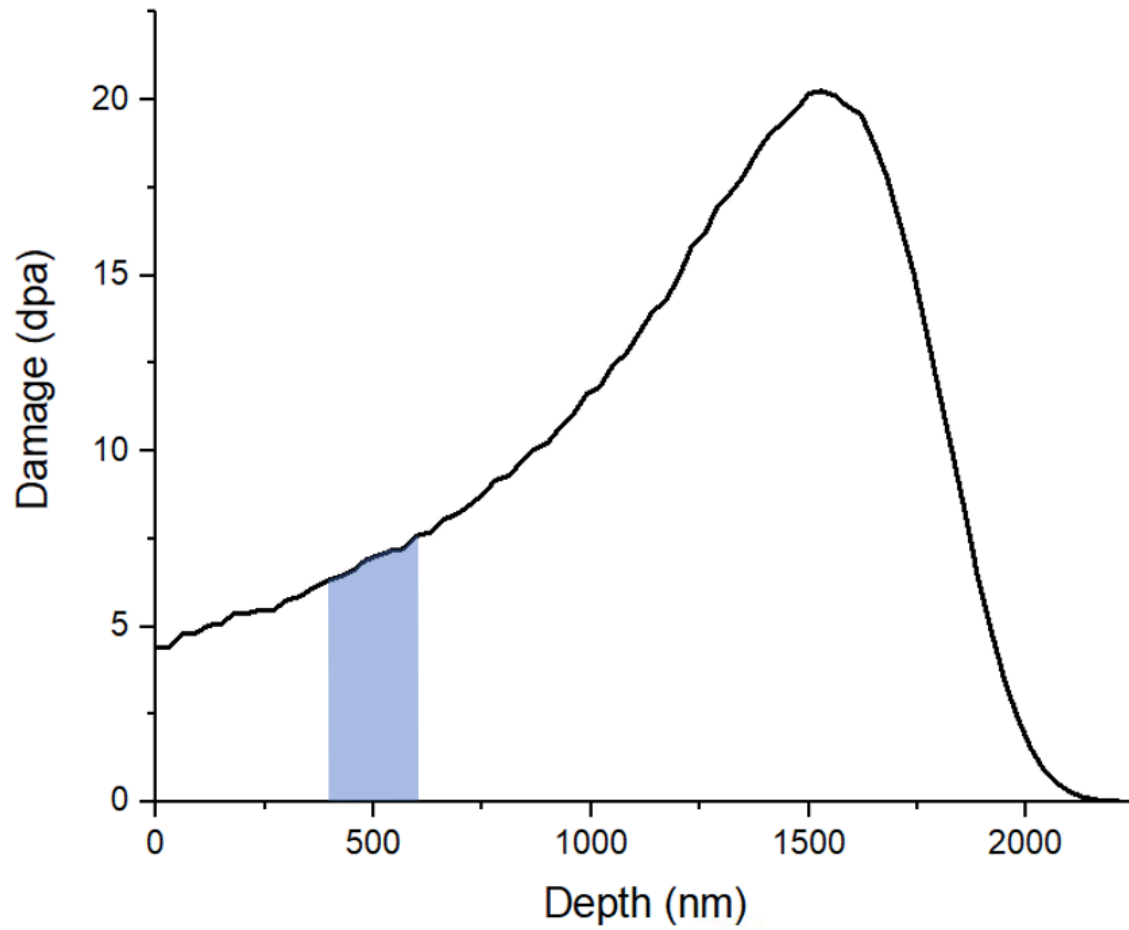


Figure 7 Ion irradiation damage profile with respect to depth as calculated from SRIM simulation. A depth of 400nm – 600nm was targeted for mechanical properties in this study (highlighted in blue).

Table 1 Composition and displacement energies used in SRIM simulation [41]

Element	Composition (at%)	Displacement Energy (eV)
Iron (Fe)	41.1	40
Chromium (Cr)	7	40
Aluminum (Al)	51.8	25

Table 2 Process and parameters for thinning TEM lamella for dislocation loop imaging

Thinning Process					
Lamella Thickness (um)	Pattern Type	Depth Dimension (um)	Voltage (kV)	Current (nA)	Time (min)
$\geq 1$	Clean Cross Section	2	30	1	-
1 - 0.5	Clean Cross Section	1	30	0.5	-
0.5 - 0.25	Clean Cross Section	0.5	30	0.3	-
0.25 - 0.15	Clean Cross Section	0.1	30	0.1	-
0.15 to Final Thickness	Clean Cross Section	0.1	30	0.049	-
Final Thickness	Rectangle	-	5	0.048	4
Final Thickness	Rectangle	-	2	0.027	2

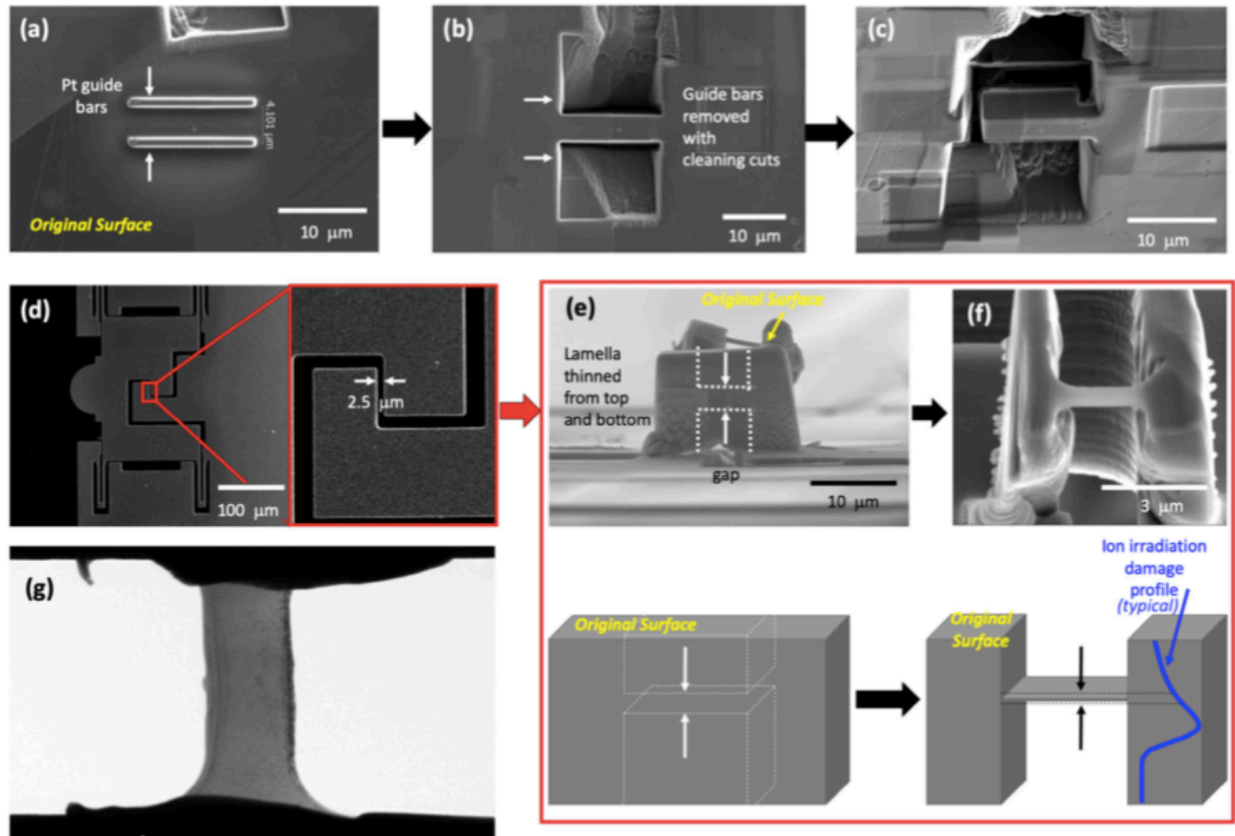


Figure 8 TEM in situ tensile sample fabrication process. (a) Location identification / sample outline, (b) FIB milling, (c) sample extraction from bulk, (d) push to pull device and location for sample placement, (e) & (f) thinning to specific depth and (g) final thinned and dogbone shaped sample [43].

Table 3 Dimensions for unirradiated and irradiated tensile samples

<u>Unirradiated</u>			
Grain Orientation	Gauge Length (um)	Width (um)	Thickness (nm)
001	1.327	0.821	122.15
	1.437	0.552	128.01
	1.465	0.375	62.47
011	1.822	0.527	89.09
	1.582	0.726	138.71
111	1.132	0.846	66.56

<u>Irradiated</u>			
Grain Orientation	Gauge Length (um)	Width (um)	Thickness (nm)
001	1.134	0.700	100.00*
011	1.041	0.653	105.34
111	1.304	0.976	98.31
	1.179	0.545	94.08

## CHAPTER 4 RESULTS

### *4.1 Microstructure*

The size of the grains ranged from a few hundred nm to tens of  $\mu\text{m}$ . The average grain size, as measured by the mean lineal intercept method, was  $4.4\mu\text{m}$ . Although there was strong texturing in different regions of the bulk material which favored a variety of different grain orientations, shown below in Figure 9 is an EBSD image displaying the grains in a region where no specific texturing was evident. Dislocation lines were quantified in the unirradiated material, and it was found that there was an areal number density of  $4.14\text{E-}5\text{m}^{-2}$ . Dislocation loops were quantified in the irradiated material, and it was found that there was a number density of  $1.12\text{E}22\text{m}^{-3}$  at a depth of 600nm into the irradiated surface with an average diameter of 12.46nm. Figure 10 & 11 shows representative TEM lamella for both conditions. The average distance between defects in the unirradiated and irradiated conditions were 41nm and 2.9nm, respectively. These data are superimposed in figure 12. The graph in figure 12 shows the likelihood that meaningful mechanical data is experimentally obtained based on defect distance vs the limiting dimension of the sample being tested.

### *4.2 Nanohardness*

The hardening was quantified by finding the difference in hardness between the unirradiated and irradiated material at a common depth. It was decided that the depth at which the difference in hardness would be measured would be 250nm due to [34] logic. The rapid decrease in hardness of the irradiated material on the hardness vs depth curve signifies the point at which the strained volume has reached / exceeded the irradiation damage peak. This depth marks the transition between the irradiated and nonirradiated hardness zones [34]. This transition occurred at 300nm which was consistent with measurements from the Yabuuchi et al paper done on BCC iron with similar irradiation conditions. The difference in hardness at 250nm was measured to be 1.13GPa for both alloys. This can be seen graphically below in Figure 12.

### *4.3 Tensile Tests*

A total of ten tensile tests were performed for the three low zone single grain orientations, namely 001, 011 and 111. In the following sections each individual test will be discussed, beginning with the unirradiated condition followed by the irradiated condition. Images of each sample before and after fracture, along with their respective stress vs strain curves can be seen below in Figures 13 – 21. Within the stress vs strain curves are marked positions at which there was an observed event in the tensile test as well as snapshots from the TEM video during the event.

#### *4.3.1 Unirradiated [001]*

Three unirradiated 001 grains were tested, two of which deformed linearly until fracturing in a brittle manner without yielding and one that yielded, and strain hardened before fracturing. The two samples that deformed linearly without yielding had different elastic moduli, with one being 58.5GPa and the other being 20GPa and their fracture stresses were 5.7GPa and 4GPa, respectively. The stiffer of these two samples did not show any sign of where the fracture would occur prior to it happening. The width of this beam was uniform throughout the entire gauged region and the elongation was uniform throughout the tensile test. Ultimately the fracture occurred near the center of the beam at an angle of 27 degrees and the total elongation was 9.7%. The gauged region on the lesser stiff beam was less wide near one end which is where the fracture took place. During the tensile test, the fracture location became less damaged and when fracture occurred it happened at an angle of 20 degrees and the total elongation was just over 20%. The sample that exhibited a clear yield point and a high degree of strain hardening appeared to be made up of two grains, with the grain boundary extending along the length of the gauged region. The modulus and yield stress for this sample were 39GPa and 470MPa, respectively, and it fractured at 1.4GPa. The fracture surface of this beam wasn't angled, but instead it was jagged and uneven until the fracture reached the second grain, where the fracture was completely horizontal. This sample had a total elongation of 7%.



#### *4.3.2 Unirradiated [011]*

The two unirradiated 011 grains that were tested behaved very differently. The first sample deformed uniformly along its gauged region until fracture. The fracture occurred in a brittle manner at the end of the gauged region at a stress of 3.3GPa. The stress vs strain curve was linear until fracture with a modulus of 22GPa. During the tensile test, similar to the unirradiated 001 grain, the region where fracture occurred becomes less damaged prior to fracture. The total elongation of this sample was 15.4%. The second sample tested exhibited deformation slip at an angle of 45 degrees. The stress vs strain curve shows yielding at 2GPa followed closely by a small strain burst and then a large increase in strain which corresponds with the slipping of the beam. The large strain burst is followed by many smaller strain bursts corresponding to more slippage at higher and higher stresses. The total elongation of this sample was about 17%.

#### *4.3.3 Unirradiated [111]*

During this test yielding occurred at 2.7GPa, a slip step formed at a stress of 2.7GPa and then at a stress of 3.4GPa and strain of 12% a band with width of 97nm appears along the length of the beam at an angle of 156 degrees. This band is believed to be a twin. At one side of the twin are microcracks that form during the stress test. Fracture occurs along the line of the twin at a strain of 15% and stress of 3.4GPa. Prior to fracture, strain hardening occurs. Load drops were observed corresponding with the slip and twin formation.

#### *4.3.4 Irradiated [001]*

One test was performed on the irradiated 001 condition. The sample yielded at about 4GPa and quickly fractured thereafter at 4.7GPa after reaching an ultimate tensile stress of 4.8GPa. The total elongation of the sample was 4.7% and the sample fractured at an angle of almost 18 degrees near the lower half of the sample.

#### *4.3.5 Irradiated [011]*

One test was performed for the irradiated 011 grain orientation. The test yielded a uniform elongation throughout the specimens gauged region, a smooth transition from the linear elastic regime to plastic deformation, slight strain hardening, followed by fracture. The fracture occurred at a slight angle of 13 degrees. The elastic modulus for this sample was 43.5GPa and the yield stress was 2.1GPa. The sample ultimately fractured at a stress of 2.4GPa with a total elongation of 6.7%. There was little evidence in the stress vs strain curves of strain bursts or stress drops.

#### *4.3.6 Irradiated [111]*

Two tests were performed for the irradiated 111 grain orientation. Both tests resulted in many visible and measurable slip events. One of the samples was much stiffer than the other and they had elastic moduli of 103.4GPa and 64.7GPa. The stiffer sample resulted in a slight strain softening of the material after yielding at 2.3GPa whereas the less stiff sample resulted in a slight strain hardening after yielding at 2GPa. During the test on the stiffer sample, slip began below where the imaging was taking place and so the image was repositioned to where the slip was happening. The sample fractured at the angle in which it was slipping which was 44 degrees. This sample produced four major events as shown in the stress vs strain curve, with the smallest being a drop in stress of 500MPa and the largest being a drop in stress of 1.7GPa. After the fourth slip event the sample failed at a stress of 1.9GPa and at a total elongation of 12%. The less stiff sample exhibited an initial stress drop of 500MPa, followed by a series of relatively small stress drops, which ranged from tens to hundreds of MPa, and finally a series of larger stress drops comparable to the initial drop when the sample finally fractured at a stress of 2.5GPa. A large slip step is formed during the test and fracture occurs along the slip step at an angle of 50 degrees after an elongation of 20.5%.

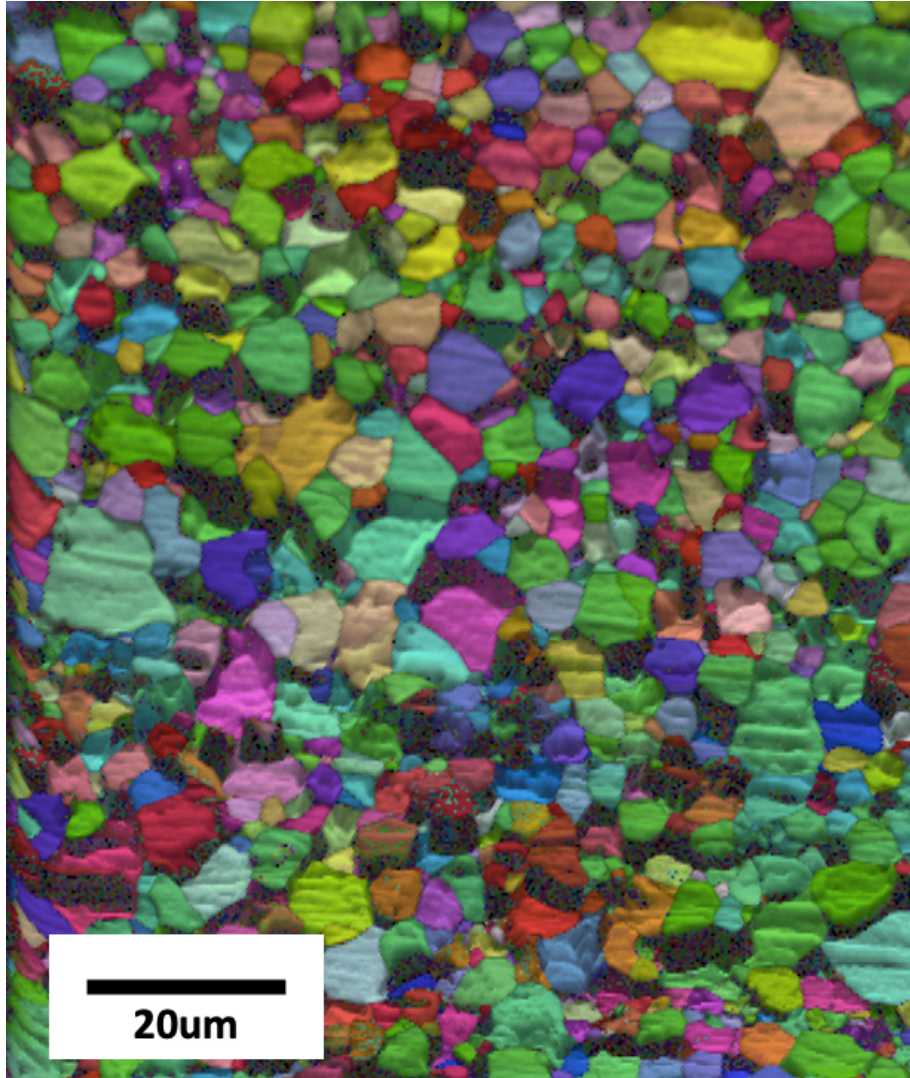


Figure 9 EBSD image displaying the grain structure and size of FeCrAl.

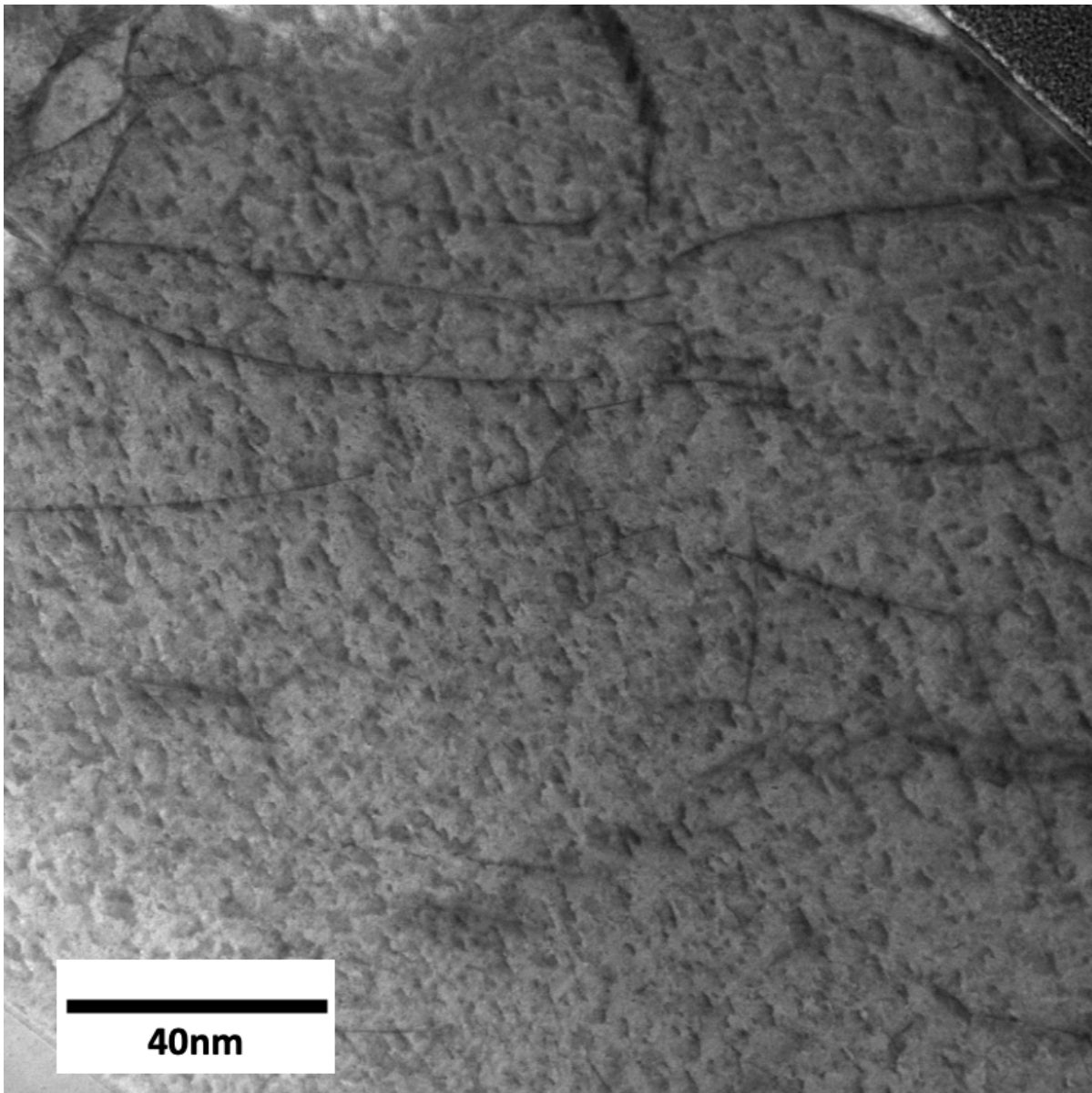


Figure 10 TEM lamella imaged using BFSTEM down the 011 zone axis. It was decided that the distributed spots were caused by FIB milling.

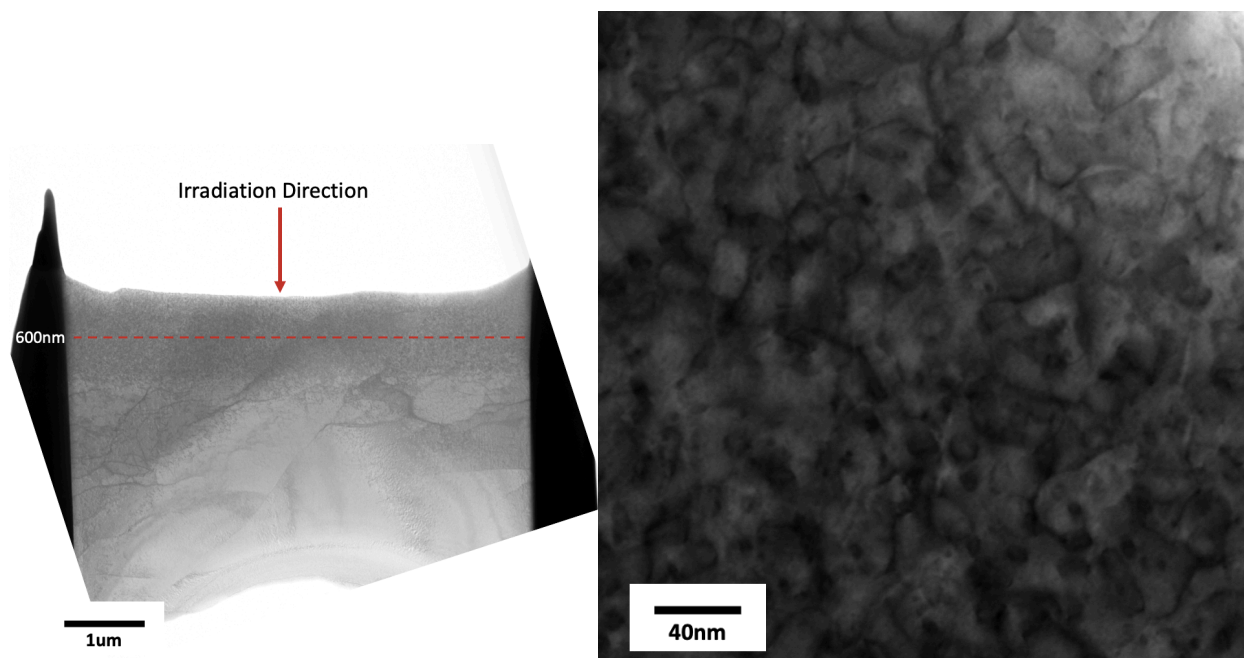


Figure 11 (left) TEM lamella imaged using BFSTEM down the 011 zone axis and (right) dislocation loops imaged 600nm into the irradiated surface.

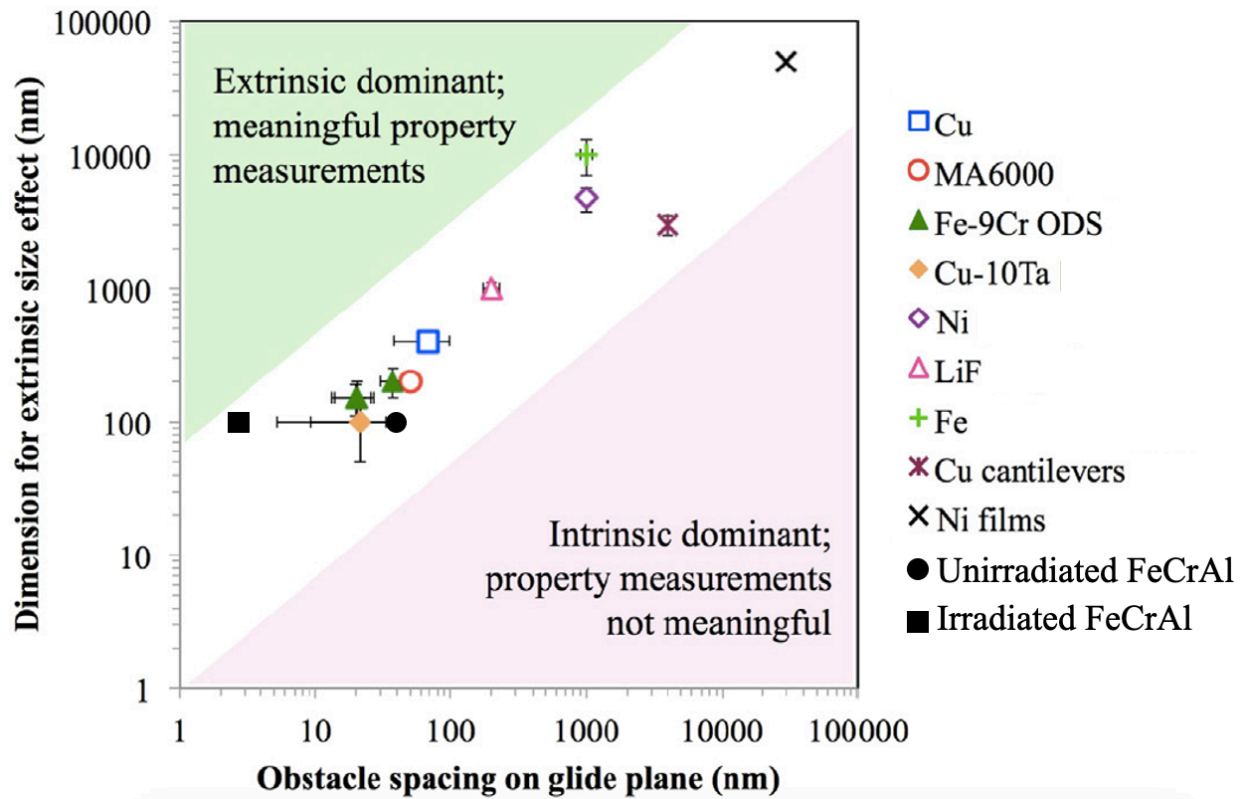


Figure 12 Unirradiated & irradiated FeCrAl microstructural data superimposed on graph displaying the relationship between extrinsic and intrinsic size effect from [43].

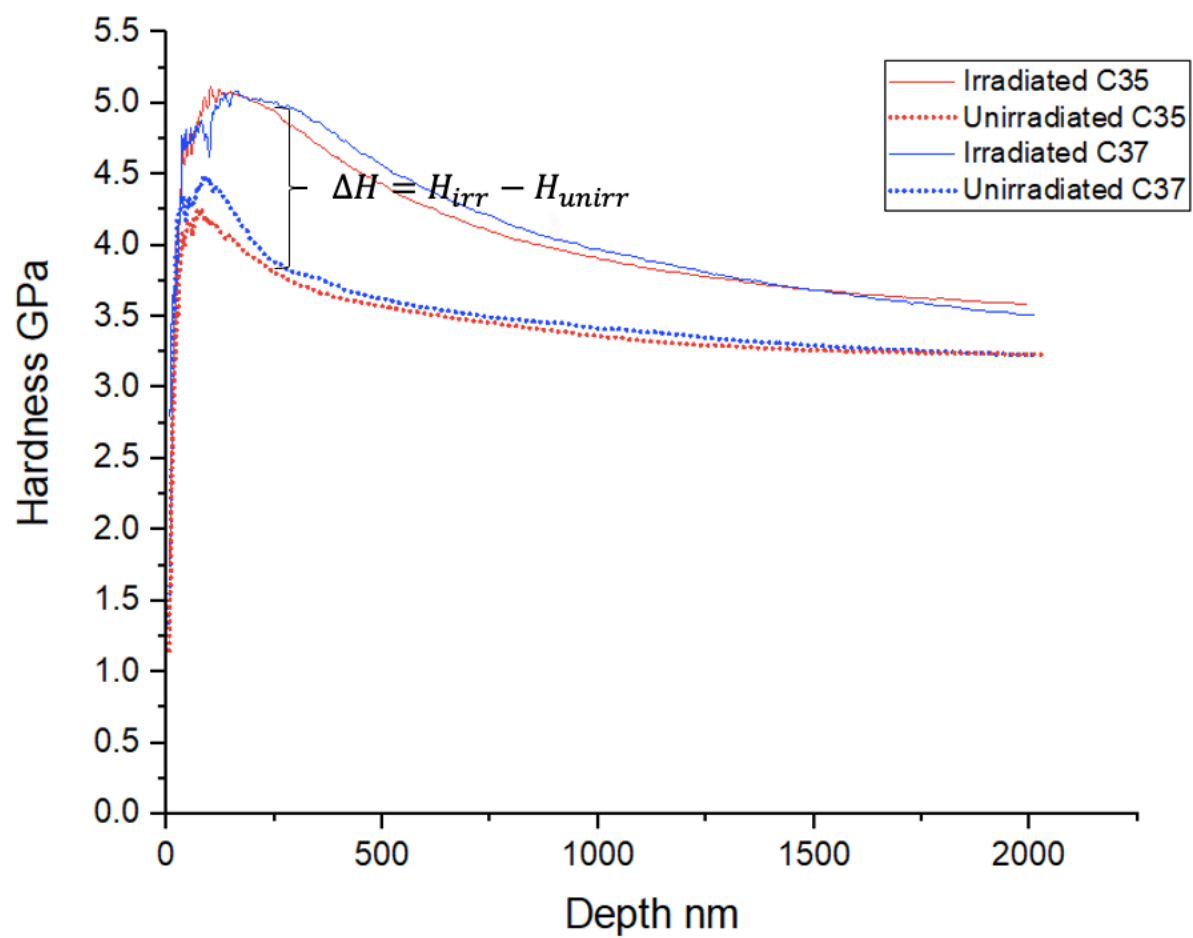


Figure 13 Nanohardness tests done on two FeCrAl alloys with 5wt% Al (red) and 7wt% Al (blue) displaying the irradiation induced hardening.



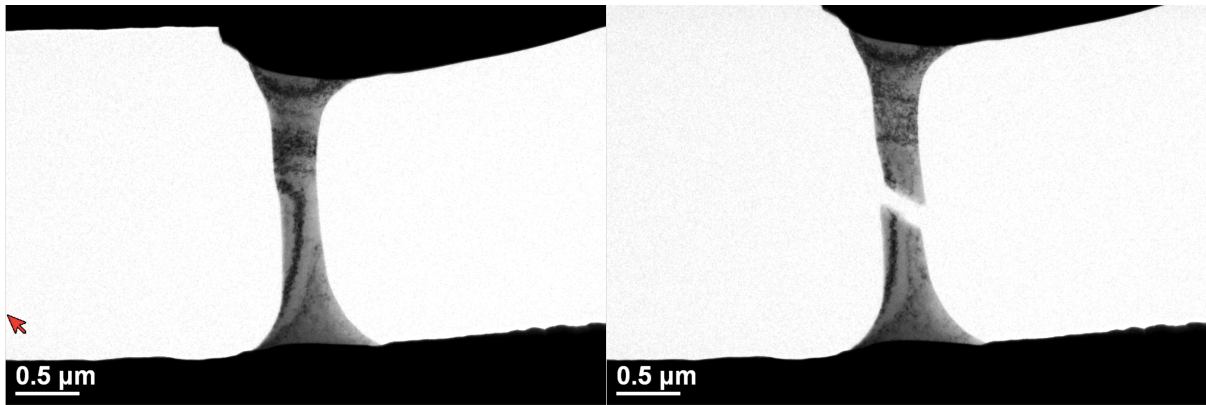
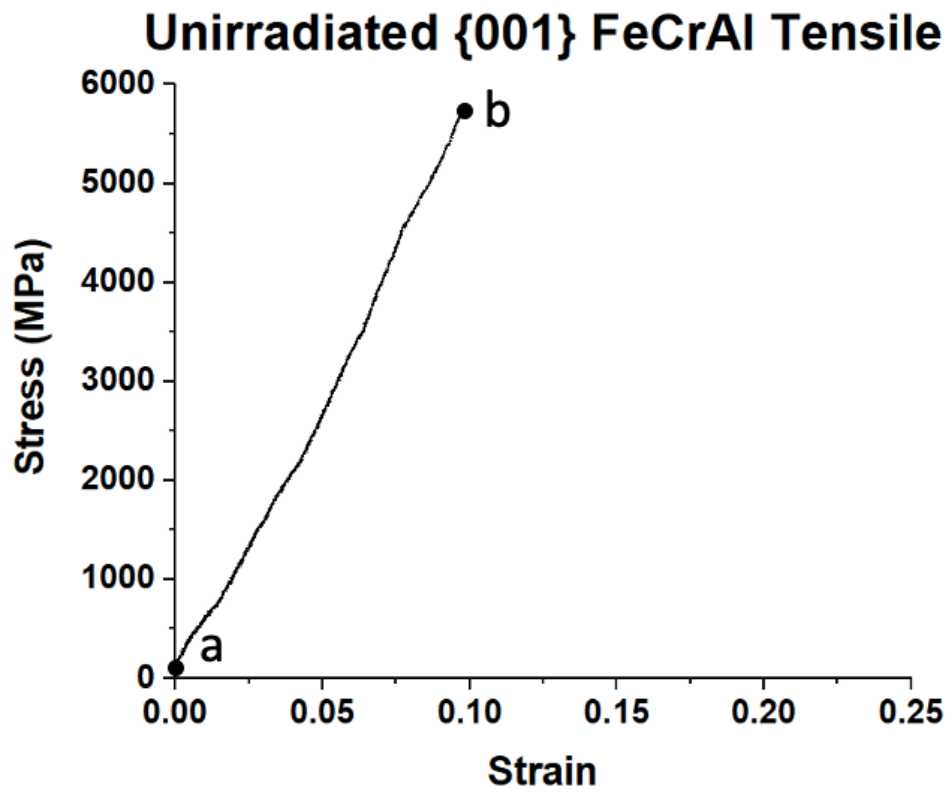


Figure 14 (above) Tensile test for unirradiated 001 grain orientation exhibiting failure after linearly deforming. (below) Still images from BFTEM video at the beginning of test and after failure.



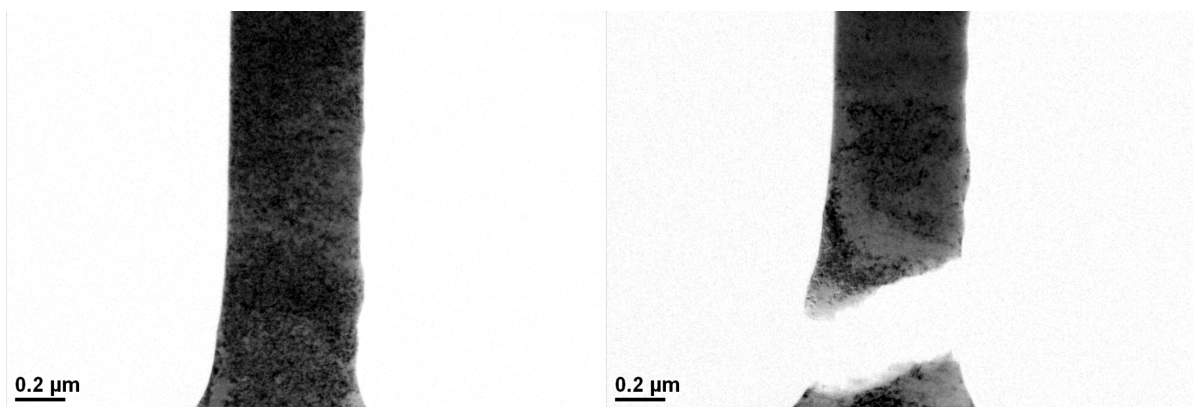
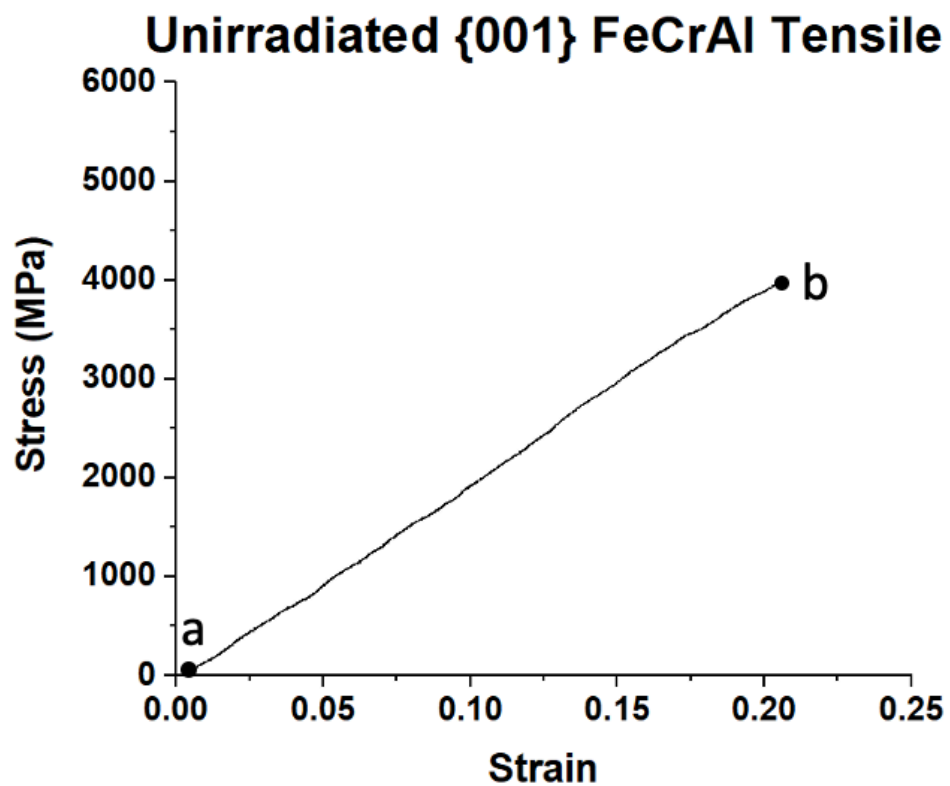


Figure 15 (above) Tensile test for unirradiated 001 grain orientation exhibiting failure after linearly deforming. (below) Still images from BFTEM video at the beginning of test and after failure.

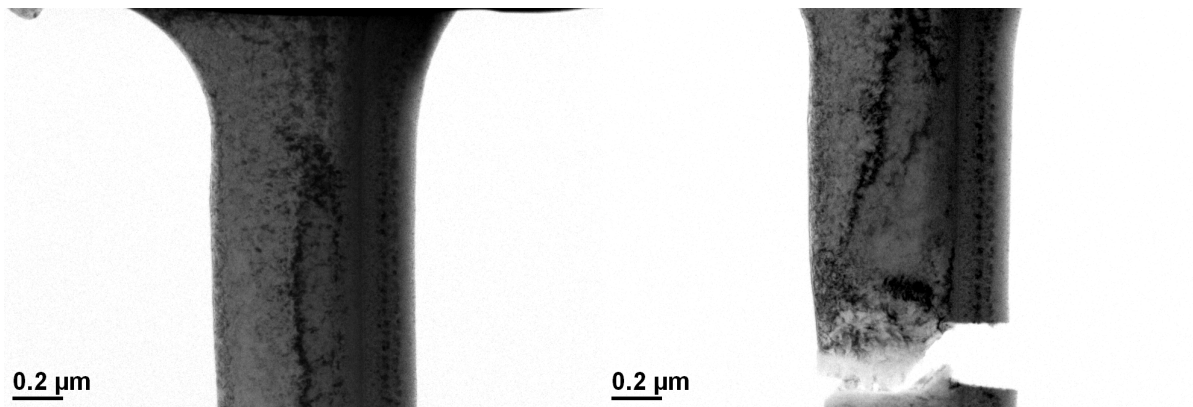
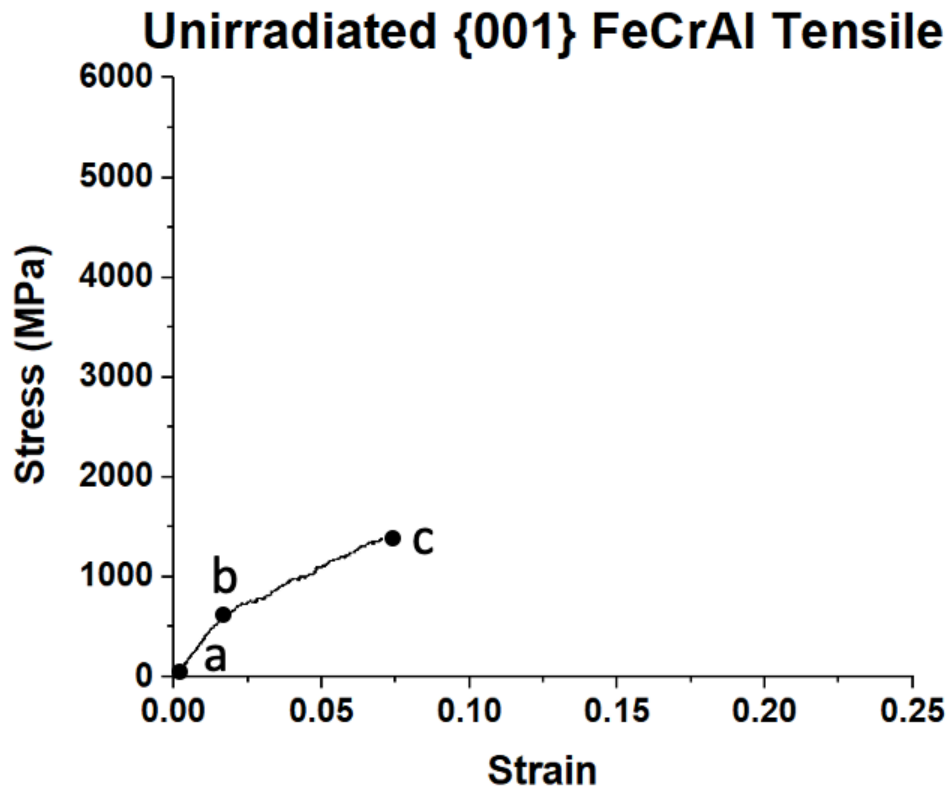


Figure 16 (above) Tensile test for unirradiated 001 grain orientation exhibiting failure after yielding.  
(below) Still images from BFTEM video at the beginning of test and after failure.

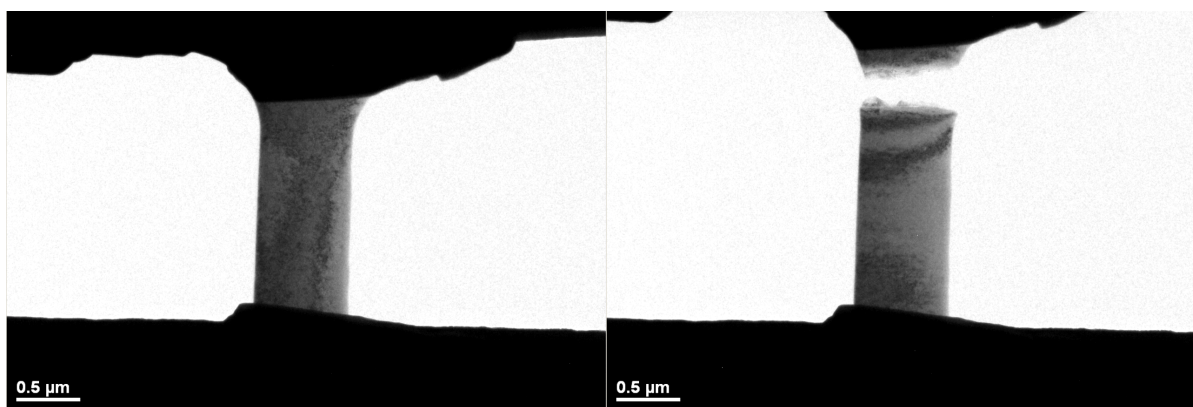
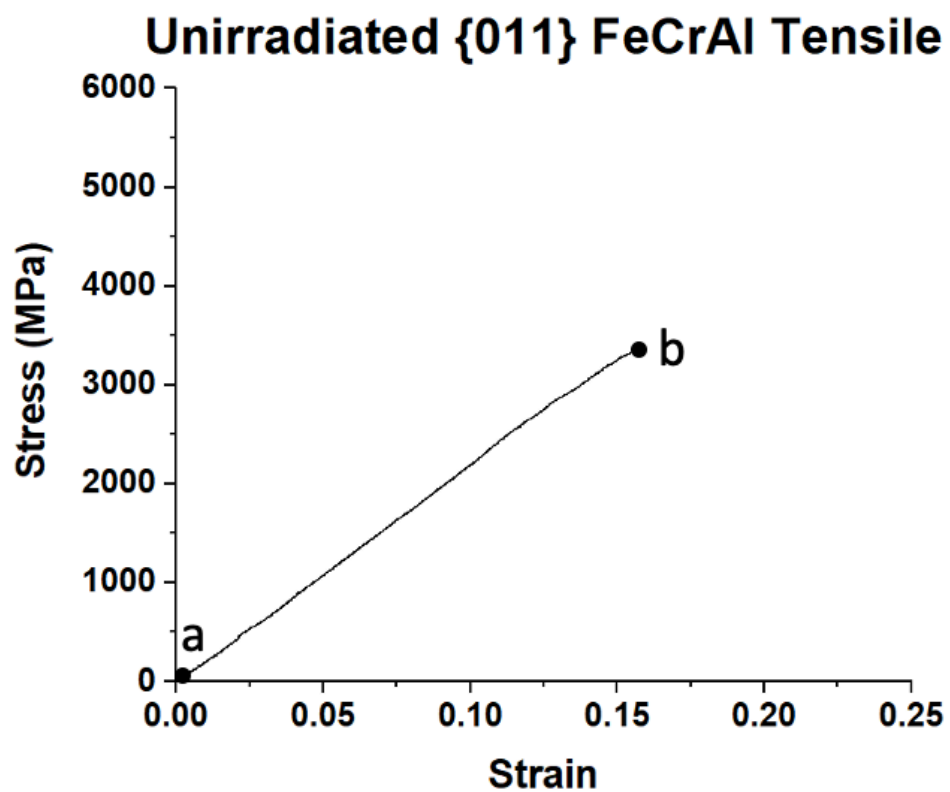


Figure 17 (above) Tensile test for unirradiated 011 grain orientation exhibiting failure after linearly deforming. (below) Still images from BFTEM video at the beginning of test and after failure.

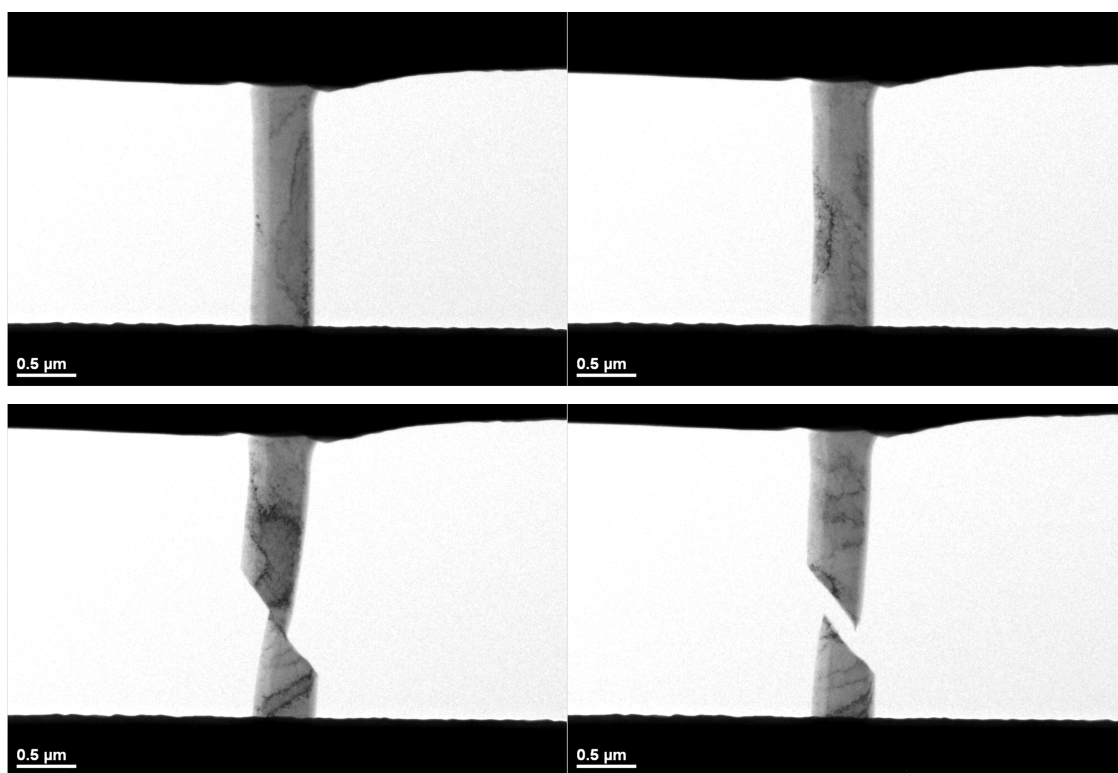
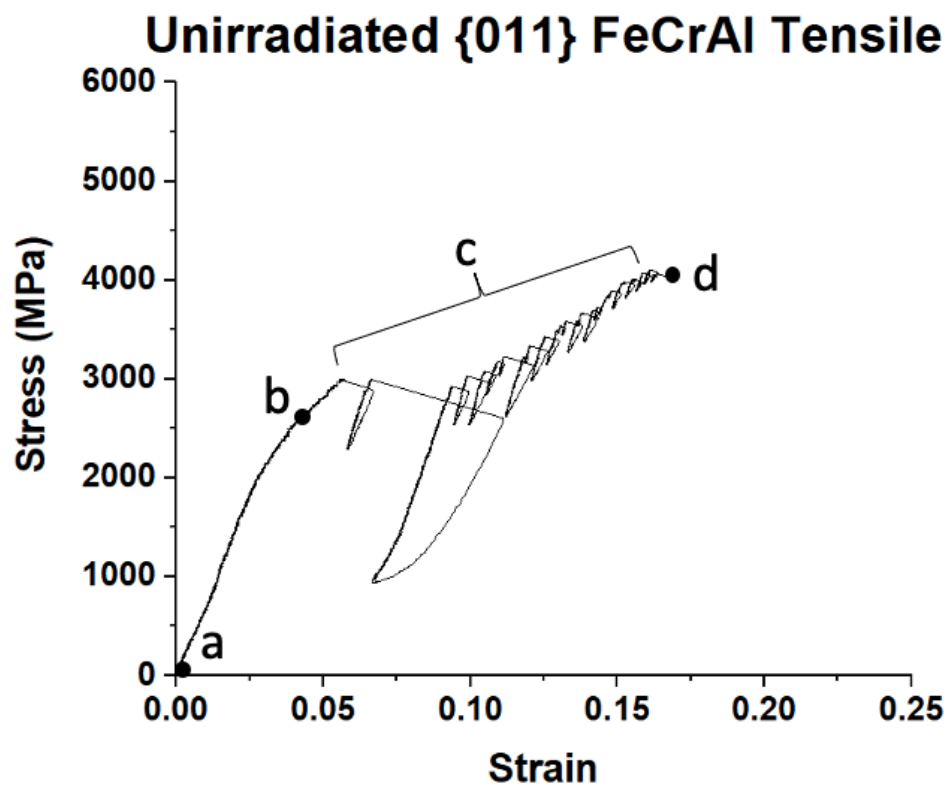


Figure 18 (above) Tensile test for unirradiated 011 grain orientation exhibiting many slip events during plastic deformation. (below) Still images from BFTEM video corresponding to beginning, yield, slip, and failure.

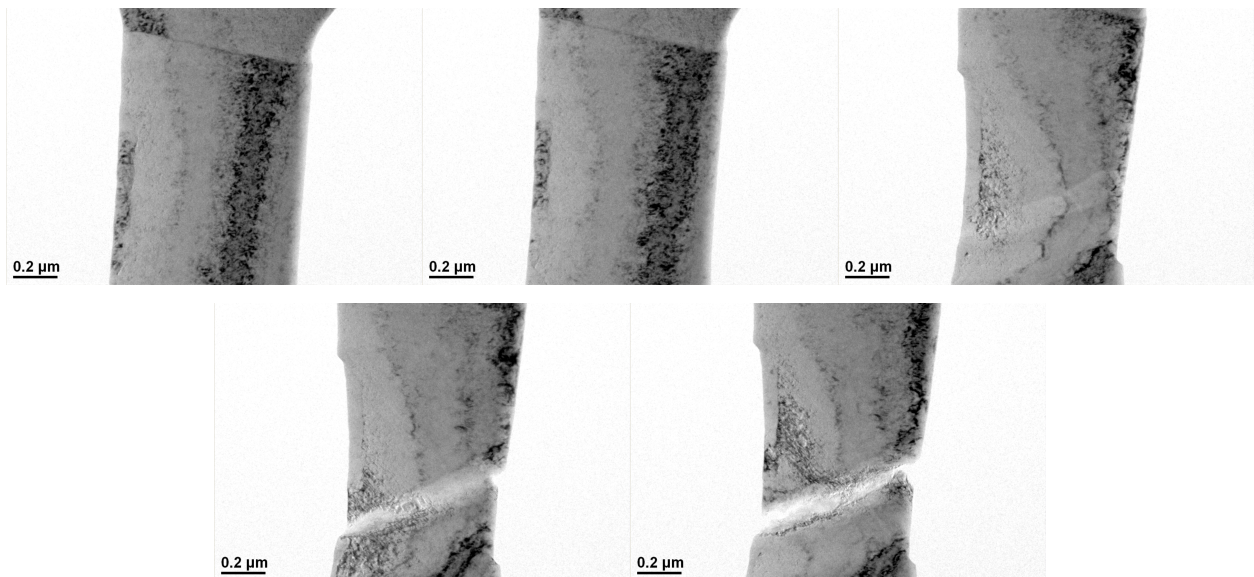
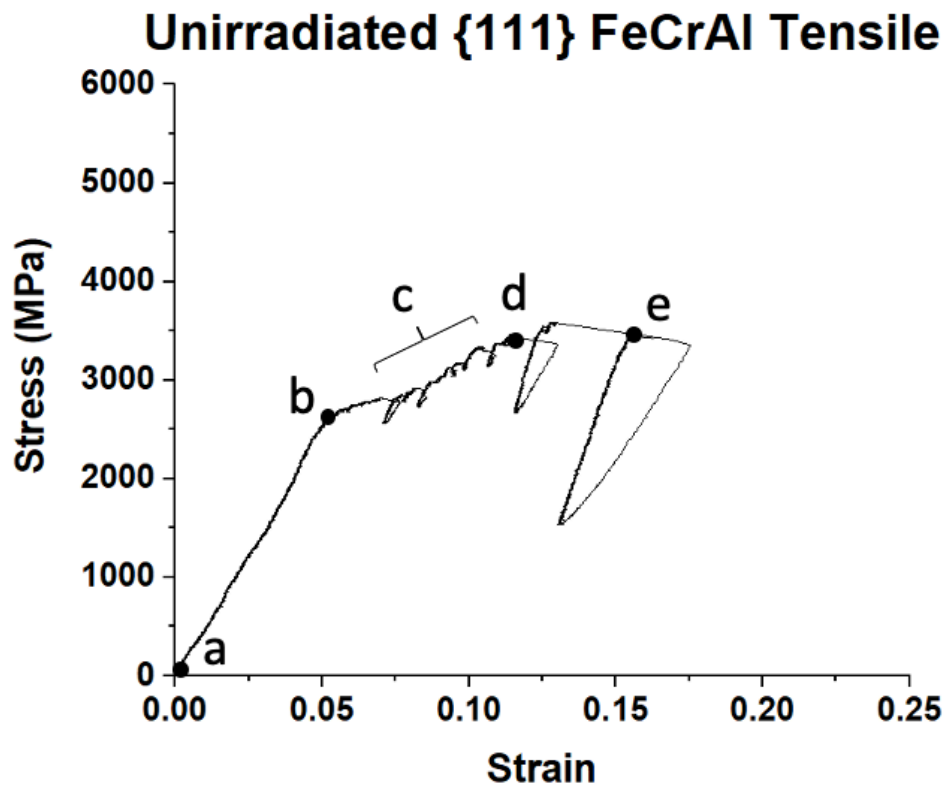


Figure 19 (above) Tensile test for unirradiated 111 grain orientation exhibiting twinning and slip. (below) Still images from BFTEM video corresponding to beginning, yield, twin formation, slip, and failure.

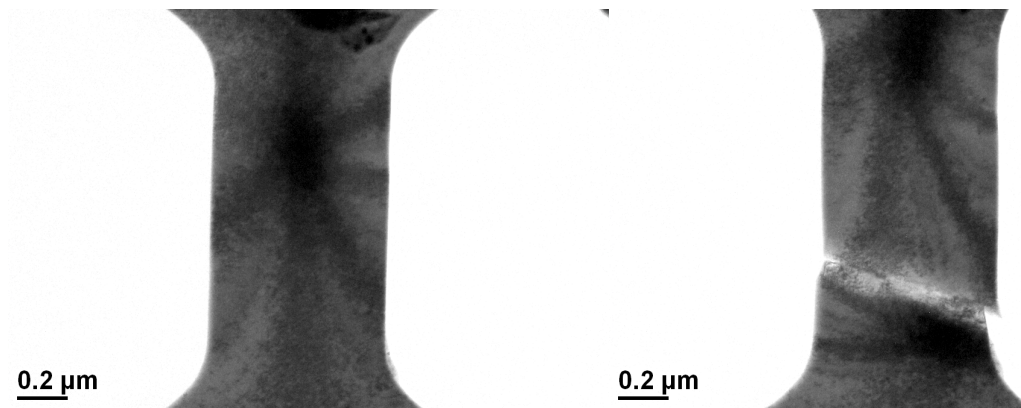
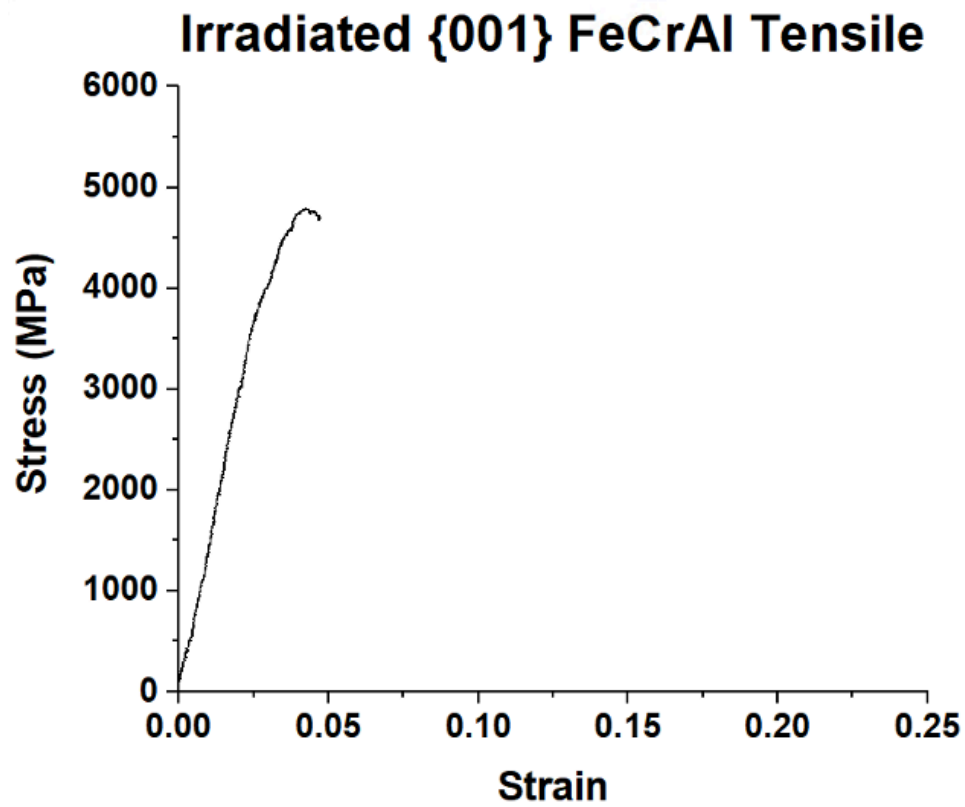


Figure 20 (above) Tensile test for irradiated 001 grain orientation exhibiting failure after yielding. (below) Still images from BFTEM video at the beginning of test and after failure.



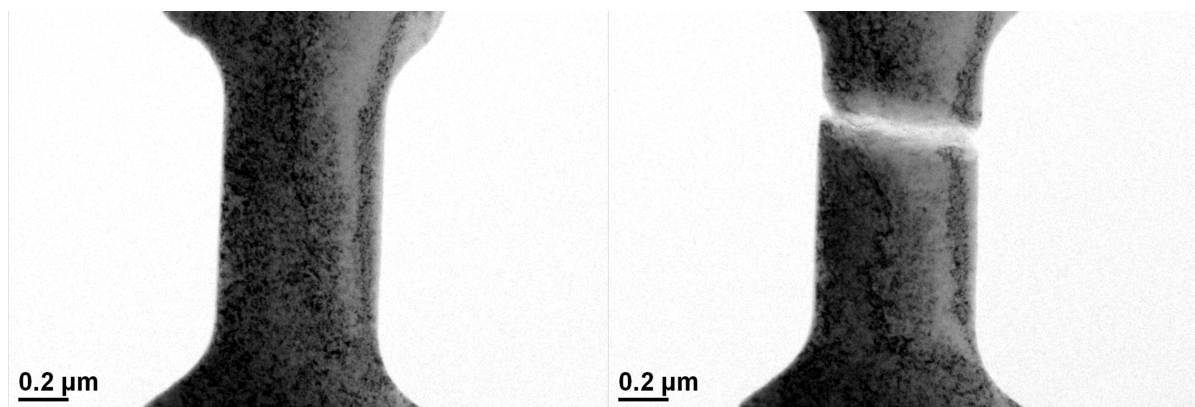
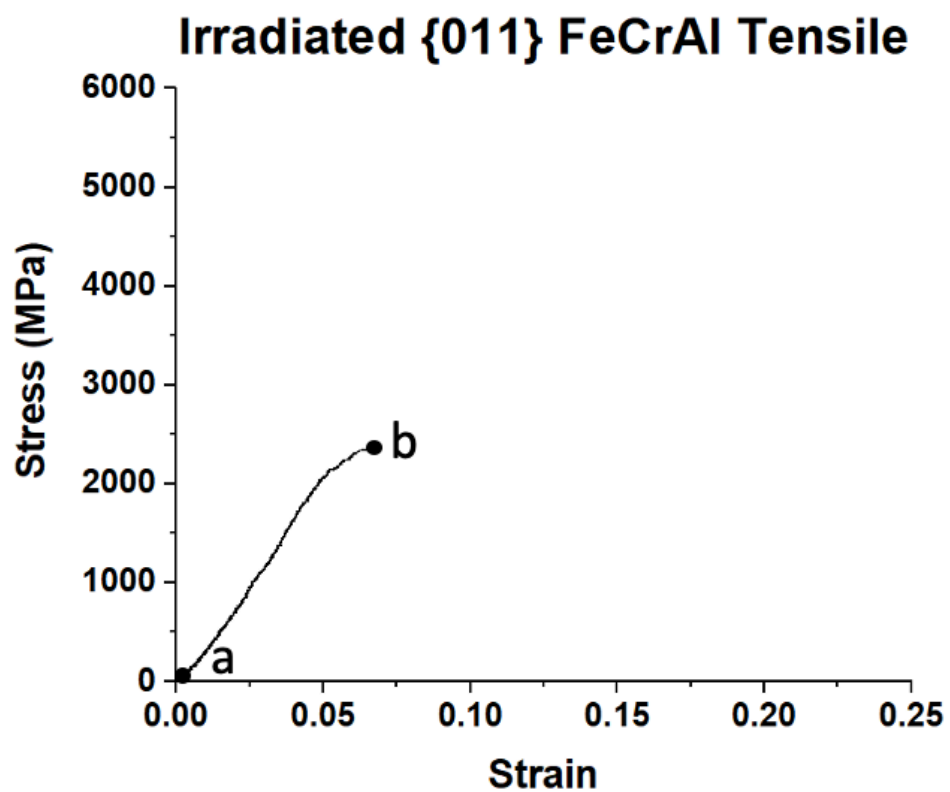


Figure 21 (above) Tensile test for irradiated 011 grain orientation exhibiting failure after yielding. (below) Still images from BFTEM video at the beginning of test and after failure.

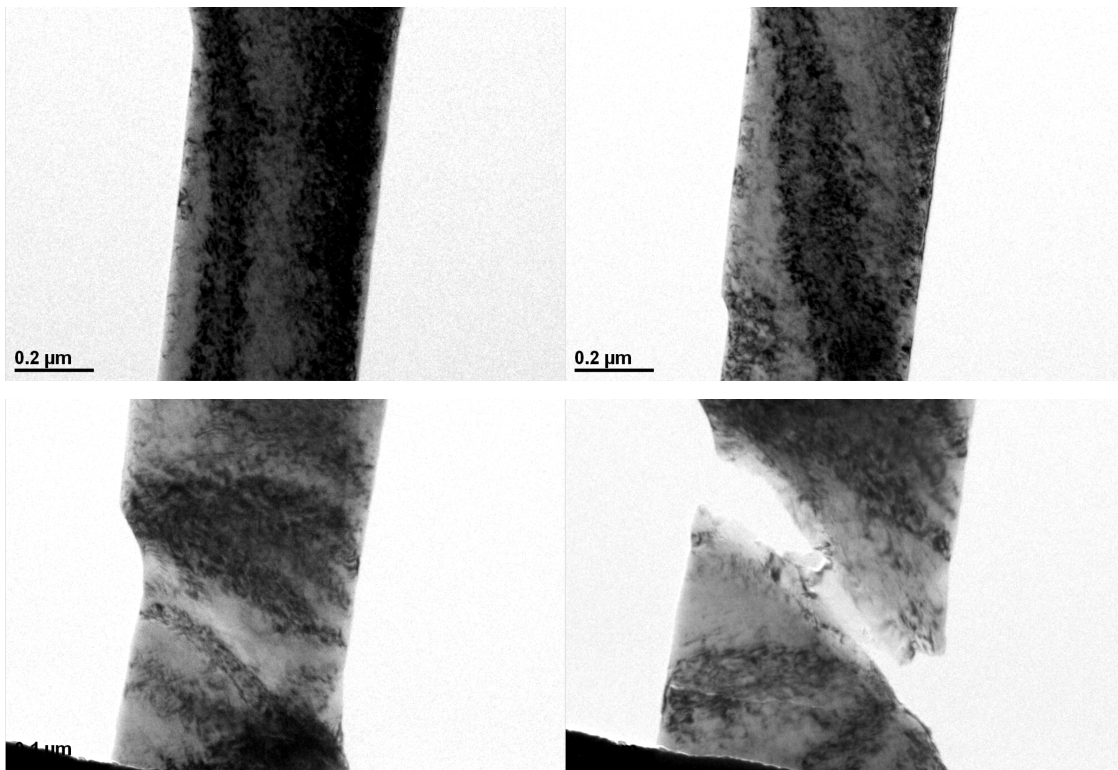
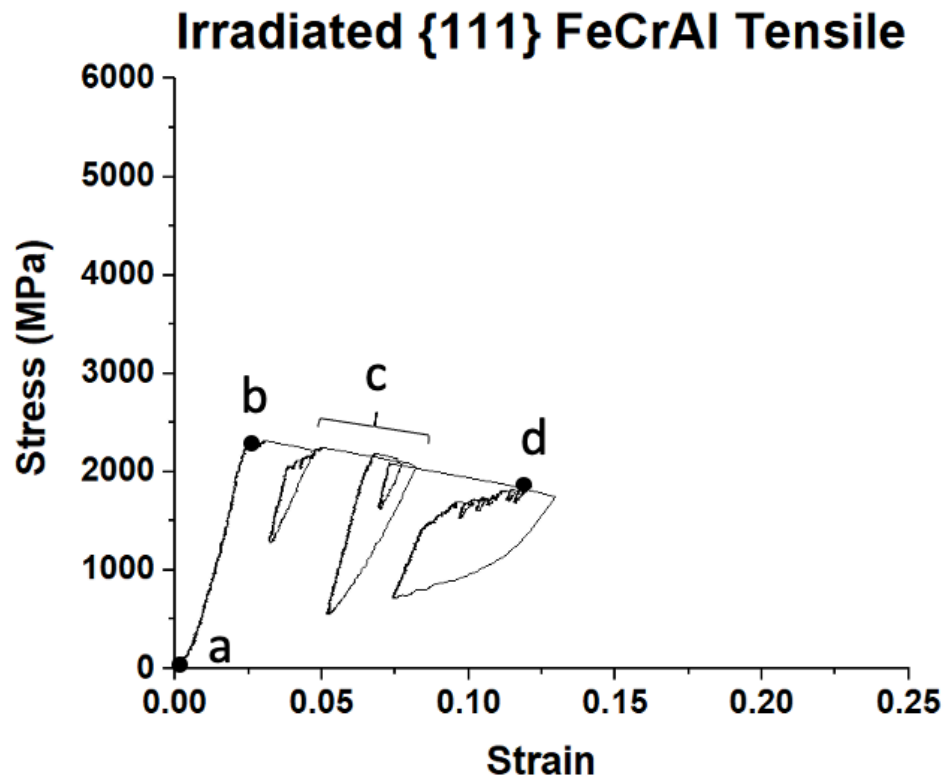


Figure 22 (above) Tensile test for irradiated 111 grain orientation exhibiting slip and softening. (below) Still images from BFTEM video corresponding to beginning, yielding, slip and failure.



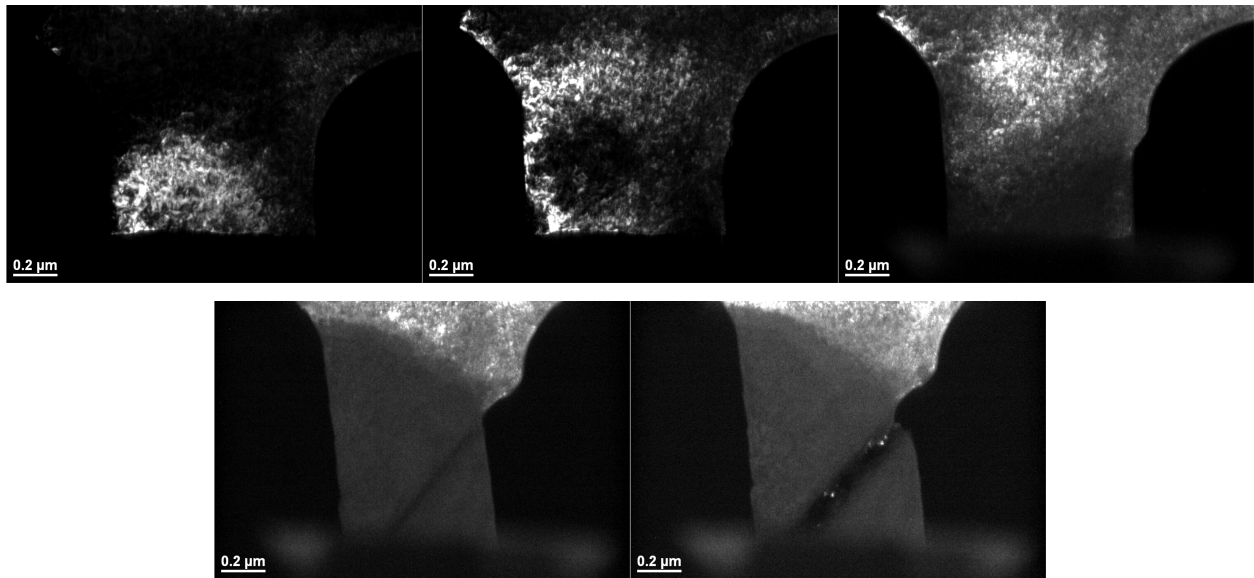
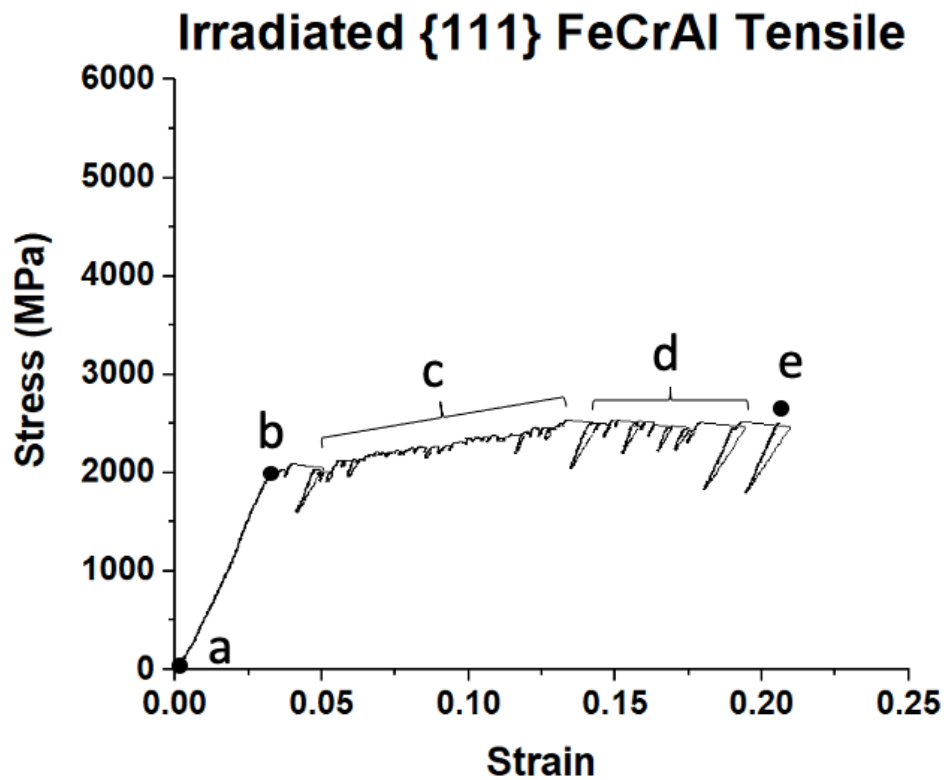


Figure 23 (above) Tensile test for irradiated 111 grain orientation exhibiting slip and slight hardening. (below) Still images from dark field TEM (DFTEM) video corresponding to beginning yield, slip and failure.

## CHAPTER 5 DISCUSSION

Until now, small scale tensile testing of unirradiated and irradiated single crystal FeCrAl alloys has not been achieved and also few small scale tests on FeCrAl alloys have been performed in general. The data collected from the tensile tests on single crystal FeCrAl provided experimental proof of the differences in strength for the three low zone crystal orientations and also the difference in strength when comparing the unirradiated to irradiated samples. The unirradiated tensile tests, in general, were stronger than their irradiated counterparts. Generally irradiated alloys tend to have higher strengths than unirradiated alloys. The fact that the irradiated tensile samples were weaker than the unirradiated samples indicates that the yield strength size effect in the irradiated samples was mitigated while the size effect still existed in the unirradiated samples. The explanation for the difference in strengths is the microstructure. In the unirradiated samples, the defect density was much lower than in the irradiated samples. For a material to plastically deform, dislocations must first exist and second must move through the materials lattice structure. In the case of the unirradiated samples, the small volume increases the likelihood that few or no defects will exist and so defects will first need to be nucleated in order to facilitate plastic deformation. In addition, the large surface area to volume ratio in these samples make it easy for defects to escape to the surface of the material, restoring the sample to its pristine condition. The lack of defects or the escaping of defects to the surface is responsible for the increased strengths because high stresses are required to nucleate defects. Another observation, independent of the irradiated condition, is the sudden stress increases and decreases, also known as strain bursts. These strain bursts can also be explained through the defects. As defects act as barriers to dislocation motion, when a dislocation meets a barrier, its motion will be impeded which will effectively cause an increase in stress. Each barrier will have a certain strength associated with it and once a sufficient stress is achieved, the dislocation will either break through or move around the barrier until it reaches another impediment which will cause a drop in stress. The stress increases and decreases will not always have the same magnitude for two main reasons. One, because the strength of each barrier will not always be the same, it will require different stresses to surpass difference barriers and two, the distance dislocations are able to glide after passing barriers will vary depending on the distance between barriers. The final observation of importance is the deformation behavior between the different crystal orientations. It was observed that in two of the three unirradiated 001

grain orientation tests brittle fracture occurred without yielding. The reason being the low density of atoms in the 001 plane and the relatively large distance between lattice atoms. The third 001 grain tested was made up of two grains and exhibited plastic deformation prior to fracture. The reason for this behavior is thought to have been the grain boundary itself. The grain boundary acts as a large two dimensional defect and a source for other dislocations which facilitated plastic deformation. The strength of the irradiated 001 sample didn't follow the general trend of being less strong than its unirradiated counterparts but it did behave differently in that it experienced yielding prior to failing. This yielding is evidence that the increased microstructural defects aided in allowing plastic deformation to occur when it otherwise wouldn't have. Another important note is that the thickness measurement for this sample was estimated due to the EELS detector being non functional at the time of testing. This is important because the sample thickness is a key parameter relating to the measured stress. The thickness was estimated to be 100nm but a small increase to this dimension would result in a much less strong sample which would lead to the sample following the general trend stated earlier. One of the unirradiated 011 grains tested slipped and one fractured without yielding. The slipping behavior is expected in this orientation because of the many slip systems that include the 011 plane. The other sample fractured at the top of the gauged region and, upon investigation, it was decided that during the FIB milling process a notch was produced at the top of the gauged region. This notch acted as a stress concentrator instead of allowing for even distribution of stress throughout the sample. The irradiated 011 grain orientations did not slip but instead yielded and quickly fractured. There are two possible reasons for this behavior. One, like the unirradiated sample, there was uneven milling and stress concentrators were created which caused a weak point in the beam or two, the increased number density of defects introduced from irradiation caused embrittlement. The 111 grain orientation, in both the unirradiated and irradiated condition, all exhibited slip behavior. The unirradiated sample was quite interesting in that it appeared to also twin prior to slipping. Twinning is known to occur in BCC materials on the 112 family of planes and because the 112 orientation is relatively close to the 111 orientations, it is likely that the sample was able to twin along the twinning plane. In this test, microcracks began to form on one end of the width. These microcracks are believed to have provided sufficient stress concentration points for partial dislocations to nucleate which subsequently led to the formation of the twin. Once the twin was formed, slipping occurred. This is believed to have happened because of the many new favorable slip systems that were provided

by the reorientation of the twin. Each of the two irradiated 111 grains slipped many times before fracture. Although the 111 plane is not a slipping plane, the 111 direction is a slipping direction, and this is the direction of tension and so it is expected that these grains would slip.

## REFERENCES

- [1] B.A. Pint, K.A. Terrani, M.P. Brady, T. Cheng, J.R. Keiser, High temperature oxidation of fuel cladding candidate materials in steam-hydrogen environments, *J. Nucl. Mater.* 440 (2013). <https://doi.org/10.1016/j.jnucmat.2013.05.047>.
- [2] B.A. Pint, K.A. Unocic, K.A. Terrani, Effect of steam on high temperature oxidation behaviour of alumina-forming alloys, *Mater. High Temp.* 32 (2015). <https://doi.org/10.1179/0960340914Z.000000000058>.
- [3] G.S. Was, R.S. Averback, Radiation damage using ion beams, in: *Compr. Nucl. Mater.*, 2012. <https://doi.org/10.1016/B978-0-08-056033-5.00007-0>.
- [4] J.I. Cole, S.M. Bruemmer, Post-irradiation deformation characteristics of heavy-ion irradiated 304L SS, *J. Nucl. Mater.* 225 (1995). [https://doi.org/10.1016/0022-3115\(94\)00672-5](https://doi.org/10.1016/0022-3115(94)00672-5).
- [5] A. Etienne, M. Hernández-Mayoral, C. Genevois, B. Radiguet, P. Pareige, Dislocation loop evolution under ion irradiation in austenitic stainless steels, *J. Nucl. Mater.* 400 (2010). <https://doi.org/10.1016/j.jnucmat.2010.02.009>.
- [6] D. Kiener, P. Hosemann, S.A. Maloy, A.M. Minor, In situ nanocompression testing of irradiated copper, *Nat. Mater.* 10 (2011). <https://doi.org/10.1038/nmat3055>.
- [7] K.H. Yano, M.J. Swenson, Y. Wu, J.P. Wharry, TEM in situ micropillar compression tests of ion irradiated oxide dispersion strengthened alloy, *J. Nucl. Mater.* 483 (2017). <https://doi.org/10.1016/j.jnucmat.2016.10.049>.
- [8] K.G. Field, Handbook on the Material Properties of FeCrAl Alloys for Nuclear Power Production Applications (FY18 Version: Revision 1), ORNL/SPR-2018/905. (2018). <https://doi.org/10.2172/1474581>.
- [9] J.C. Haley, S.A. Briggs, P.D. Edmondson, K. Sridharan, S.G. Roberts, S. Lozano-Perez, K.G. Field, Dislocation loop evolution during in-situ ion irradiation of model FeCrAl alloys, *Acta Mater.* 136 (2017). <https://doi.org/10.1016/j.actamat.2017.07.011>.
- [10] K.G. Field, X. Hu, K.C. Littrell, Y. Yamamoto, L.L. Snead, Radiation tolerance of neutron-irradiated model Fe-Cr-Al alloys, *J. Nucl. Mater.* 465 (2015). <https://doi.org/10.1016/j.jnucmat.2015.06.023>.

- [11] A. Bhattacharya, E. Meslin, J. Henry, A. Barbu, S. Poissonnet, B. Décamps, Effect of chromium on void swelling in ion irradiated high purity Fe-Cr alloys, *Acta Mater.* 108 (2016). <https://doi.org/10.1016/j.actamat.2016.02.027>.
- [12] E.A. Little, D.A. Stow, Void-swelling in irons and ferritic steels, *J. Nucl. Mater.* 87 (1979). [https://doi.org/10.1016/0022-3115\(79\)90123-5](https://doi.org/10.1016/0022-3115(79)90123-5).
- [13] Y. Katoh, A. Kohyama, D.S. Gelles, Swelling and dislocation evolution in simple ferritic alloys irradiated to high fluence in FFTF/MOTA, *J. Nucl. Mater.* 225 (1995). [https://doi.org/10.1016/0022-3115\(94\)00669-5](https://doi.org/10.1016/0022-3115(94)00669-5).
- [14] Y. Cui, E. Aydogan, J.G. Gigax, Y. Wang, A. Misra, S.A. Maloy, N. Li, In Situ Micro-Pillar Compression to Examine Radiation-Induced Hardening Mechanisms of FeCrAl Alloys, *Acta Mater.* 202 (2021). <https://doi.org/10.1016/j.actamat.2020.10.047>.
- [15] D. Xie, B. Wei, W. Wu, J. Wang, Crystallographic orientation dependence of mechanical responses of fecral micropillars, *Crystals*. 10 (2020). <https://doi.org/10.3390/cryst10100943>.
- [16] W.D. Callister, *Materials science and engineering: An introduction* (2nd edition), Mater. Des. 12 (1991). [https://doi.org/10.1016/0261-3069\(91\)90101-9](https://doi.org/10.1016/0261-3069(91)90101-9).
- [17] G. Sainath, B.K. Choudhary, Orientation dependent deformation behaviour of BCC iron nanowires, *Comput. Mater. Sci.* 111 (2016). <https://doi.org/10.1016/j.commatsci.2015.09.055>.
- [18] D. Zhang, L. Jiang, B. Zheng, J.M. Schoenung, S. Mahajan, E.J. Lavernia, I.J. Beyerlein, J.M. Schoenung, E.J. Lavernia, Deformation Twinning (Update), in: *Ref. Modul. Mater. Sci. Mater. Eng.*, 2016. <https://doi.org/10.1016/b978-0-12-803581-8.02878-2>.
- [19] A.W. Sleeswyk, Perfect dislocation pole models for twinning in the f.c.c. and b.c.c. lattices, *Philos. Mag.* 29 (1974). <https://doi.org/10.1080/14786437408213281>.
- [20] K. Ogawa, Edge dislocations dissociated in (112) planes and twinning mechanism of b.c.c. metals, *Philos. Mag.* 11 (1965). <https://doi.org/10.1080/14786436508221852>.
- [21] S. Li, X. Ding, J. Deng, T. Lookman, J. Li, X. Ren, J. Sun, A. Saxena, Superelasticity in bcc nanowires by a reversible twinning mechanism, *Phys. Rev. B - Condens. Matter Mater. Phys.* 82 (2010). <https://doi.org/10.1103/PhysRevB.82.205435>.
- [22] J. Luo, Study of microcrack nucleation from a blocked twin with the wedge disclination model, *Arch. Appl. Mech.* 87 (2017). <https://doi.org/10.1007/s00419-016-1177-x>.

- [23] L. Liu, H.C. Wu, J. Wang, S.K. Gong, S.X. Mao, Twinning-dominated nucleation, propagation and deflection of crack in molybdenum characterized with in situ transmission electron microscopy, *Philos. Mag. Lett.* 94 (2014). <https://doi.org/10.1080/09500839.2014.886783>.
- [24] G. Sainath, B.K. Choudhary, T. Jayakumar, Molecular dynamics simulation studies on the size dependent tensile deformation and fracture behaviour of body centred cubic iron nanowires, *Comput. Mater. Sci.* 104 (2015). <https://doi.org/10.1016/j.commatsci.2015.03.053>.
- [25] G.S. Was, *Fundamentals of radiation materials science: Metals and alloys*, second edition, 2016. <https://doi.org/10.1007/978-1-4939-3438-6>.
- [26] D.J. Mazey, Fundamental aspects of high-energy ion-beam simulation techniques and their relevance to fusion materials studies, *J. Nucl. Mater.* 174 (1990). [https://doi.org/10.1016/0022-3115\(90\)90234-E](https://doi.org/10.1016/0022-3115(90)90234-E).
- [27] S. Ishino, N. Sekimura, Role of charged particle irradiations in the study of radiation damage correlation, *J. Nucl. Mater.* 174 (1990). [https://doi.org/10.1016/0022-3115\(90\)90230-K](https://doi.org/10.1016/0022-3115(90)90230-K).
- [28] G.S. Was, T.R. Allen, RADIATION DAMAGE FROM DIFFERENT PARTICLE TYPES, in: *Radiat. Eff. Solids*, 2007. [https://doi.org/10.1007/978-1-4020-5295-8\\_4](https://doi.org/10.1007/978-1-4020-5295-8_4).
- [29] K.G. Field, S.A. Briggs, K. Sridharan, Y. Yamamoto, R.H. Howard, Dislocation loop formation in model FeCrAl alloys after neutron irradiation below 1 dpa, *J. Nucl. Mater.* 495 (2017). <https://doi.org/10.1016/j.jnucmat.2017.07.061>.
- [30] P.D. Edmondson, S.A. Briggs, Y. Yamamoto, R.H. Howard, K. Sridharan, K.A. Terrani, K.G. Field, Irradiation-enhanced  $\alpha'$  precipitation in model FeCrAl alloys, *Scr. Mater.* 116 (2016). <https://doi.org/10.1016/j.scriptamat.2016.02.002>.
- [31] K. Mao, G. Maxim, C. Massey, K. Unocic, P. Edmondson, K. Field, In-situ Micromechanical Testing of Neutron Irradiated FeCrAl Alloys, *Microsc. Microanal.* 26 (2020). <https://doi.org/10.1017/s1431927620015391>.
- [32] M.N. Gushev, E. Cakmak, K.G. Field, Impact of neutron irradiation on mechanical performance of FeCrAl alloy laser-beam weldments, *J. Nucl. Mater.* 504 (2018). <https://doi.org/10.1016/j.jnucmat.2018.03.036>.

- [33] K.G. Field, S.A. Briggs, X. Hu, Y. Yamamoto, R.H. Howard, K. Sridharan, Heterogeneous dislocation loop formation near grain boundaries in a neutron-irradiated commercial FeCrAl alloy, *J. Nucl. Mater.* 483 (2017). <https://doi.org/10.1016/j.jnucmat.2016.10.050>.
- [34] K. Yabuuchi, R. Kasada, A. Kimura, Effect of alloying elements on irradiation hardening behavior and microstructure evolution in BCC Fe, *J. Nucl. Mater.* 442 (2013). <https://doi.org/10.1016/j.jnucmat.2013.04.035>.
- [35] D. Li, H. Zbib, X. Sun, M. Khaleel, Predicting plastic flow and irradiation hardening of iron single crystal with mechanism-based continuum dislocation dynamics, *Int. J. Plast.* 52 (2014). <https://doi.org/10.1016/j.ijplas.2013.01.015>.
- [36] S. Papanikolaou, Y. Cui, N. Ghoniem, Avalanches and plastic flow in crystal plasticity: An overview, *Model. Simul. Mater. Sci. Eng.* 26 (2018). <https://doi.org/10.1088/1361-651X/aa97ad>.
- [37] S.H. Oh, M. Legros, D. Kiener, G. Dehm, In situ observation of dislocation nucleation and escape in a submicrometre aluminium single crystal, *Nat. Mater.* 8 (2009). <https://doi.org/10.1038/nmat2370>.
- [38] T.A. Parthasarathy, S.I. Rao, D.M. Dimiduk, M.D. Uchic, D.R. Trinkle, Contribution to size effect of yield strength from the stochastics of dislocation source lengths in finite samples, *Scr. Mater.* 56 (2007). <https://doi.org/10.1016/j.scriptamat.2006.09.016>.
- [39] Y. Cui, The Investigation of Plastic Behavior by Discrete Dislocation Dynamics for Single Crystal Pillar at Submicron Scale, 2017.
- [40] J.F. Ziegler, M.D. Ziegler, J.P. Biersack, SRIM - The stopping and range of ions in matter (2010), *Nucl. Instruments Methods Phys. Res. Sect. B Beam Interact. with Mater. Atoms.* 268 (2010). <https://doi.org/10.1016/j.nimb.2010.02.091>.
- [41] L.A. Giannuzzi, J.L. Drown, S.R. Brown, R.B. Irwin, F.A. Stevie, Applications of the FIB lift-out technique for TEM specimen preparation, *Microsc. Res. Tech.* 41 (1998). [https://doi.org/10.1002/\(SICI\)1097-0029\(19980515\)41:4<285::AID-JEMT1>3.0.CO;2-Q](https://doi.org/10.1002/(SICI)1097-0029(19980515)41:4<285::AID-JEMT1>3.0.CO;2-Q).
- [42] P.H. Warren, G. Warren, M. Dubey, J. Burns, Y.Q. Wu, J.P. Wharry, Method for Fabricating Depth-Specific TEM In Situ Tensile Bars, *JOM.* 72 (2020). <https://doi.org/10.1007/s11837-020-04105-8>.



- [43] J.P. Wharry, K.H. Yano, P. V. Patki, Intrinsic-extrinsic size effect relationship for micromechanical tests, *Scr. Mater.* 162 (2019). <https://doi.org/10.1016/j.scriptamat.2018.10.045>.